



Dendrimer functionalized carbon quantum dot for selective detection of breast cancer and gene therapy

Santanu Ghosh, Krishanu Ghosal, Sk Arif Mohammad, Kishor Sarkar*

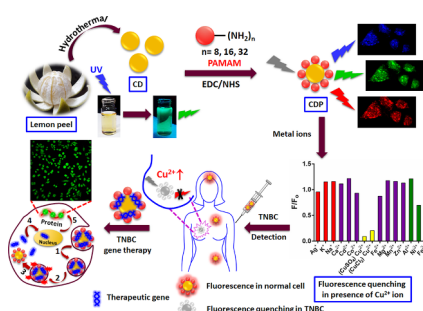
Gene Therapy and Tissue Engineering Lab, Department of Polymer Science and Technology, University of Calcutta, 92, A.P.C. Road, Kolkata 700009, India



HIGHLIGHTS

- Green synthesis of carbon quantum dot (CD) from sweet lemon peel waste.
- Amine functionalization of CDs (CDP) through conjugation of PAMAM dendrimer.
- Efficient targeted gene transfection efficiency in triple negative breast cancer.
- Highly selective detection of Cu(II) ion with 93% quenching efficiency.
- CDP may be promising theranostic tool for TNBC patient.

GRAPHICAL ABSTRACT



ARTICLE INFO

Keywords:

Carbon quantum dot
PAMAM dendrimer
Triple negative breast cancer
Gene delivery
Copper detection

ABSTRACT

Triple negative breast cancer (TNBC) is the most fatal subtype among all other types of breast cancer and there are no targeted chemotherapy for the treatment of TNBC due to the absence of estrogen receptor (ER), progesterone receptor (PR) and human epidermal growth factor receptor-2 (HER-2). To address this problem, we develop a targeted non-viral vector which could efficiently deliver the gene of interest and could also diagnose of TNBC. We have synthesized carbon quantum dots (CD) from sweet lemon peel, conjugated it with different generation of polyamidoamine (PAMAM) dendrimers to get CD-PAMAM conjugates (CDPs). RGDS peptide was further conjugated to CDP to target $\alpha_v\beta_3$ integrin which is over expressed in TNBC. DNA complexation assay, cellular cytotoxicity, hemolysis assay, DNase I assay, cellular uptake and *in vitro* transfection showed CDP3 as a promising gene carrier system TNBC gene therapy. Besides, CDP3 shows selective quenching of fluorescence in presences of Cu(II) with a quenching efficiency of about 93%. As the Cu(II) ion concentration remains up-regulated in TNBC, CDP3 could be a promising theranostic tool for TNBC treatment.

1. Introduction

Breast cancer is the second leading cause of death in women worldwide [1]. Among the different types of breast cancers diagnosed, triple negative breast cancer (TNBC) accounts about nearly 10–15% in women having the average age within 53 years. Due to the absence of estrogen receptor (ER), progesterone receptor (PR) and human

epidermal growth factor receptor-2 (HER-2), the diagnosis and treatment of TNBC patient are remain challenging which results high relapse rate, short progression-free survival (PFS) and overall survival (OS) [2]. TNBC is most aggressive type of cancer having relapse rate less than 5 years [3,4]. However, metastases are the major issues of TNBC which makes this subtype of breast cancer more fatal. In a search for the proteins and the signaling pathways involved in tumor cell malignancy,

* Corresponding author.

E-mail addresses: kishorpst@gmail.com, kspoly@caluniv.ac.in (K. Sarkar).

URL: <http://kishorgttl.com> (K. Sarkar).

<https://doi.org/10.1016/j.cej.2019.05.023>

Received 15 February 2019; Received in revised form 26 April 2019; Accepted 6 May 2019

Available online 09 May 2019

1385-8947/ © 2019 Elsevier B.V. All rights reserved.

MacDonald et al. [5] found that Memo is an essential enzyme for the breast cancer cell motility in association of various receptor tyrosine kinases. They also showed that Memo is a metal-binding enzyme which utilizes Cu(II) ion for its oxidase activity. They further noticed that Memo increases the local reactive oxygen species (ROS) production only in the presence of Cu(II) ion among the eight different cations and results cell migration and finally metastasis. Therefore, Cu(II) ion has an important role on tumor growth and angiogenesis. Apart from Memo, some other proteins such as MeK1 [6], LOX [7] and SPARC [8] were also identified which also have an important role in cancer metastases in presence of Cu(II) ions. Finney et al. also revealed that around 80–90% of total copper ion accumulates in the intracellular compartment during angiogenesis [9]. In a recent clinical study conducted by Pavithra group showed that the copper ion concentration in serum increased significantly from 110 µg/dL to 202 µg/dL in breast cancer patients compared to healthy women [10]. Therefore, a highly selective and sensitive biosensor for copper ion detection may be an attractive diagnostic tool for TNBC patients.

Despite the tremendous progress in cancer research, chemotherapy still remains the most widely used clinical therapy of any type of cancer including TNBC. Due to severe side effect of chemotherapy, researchers are trying to find out alternate therapeutic approach for cancer treatment. Recently, theranostic approach has gained remarkable attention in biomedical field due its simultaneous diagnosis and treatment concept [11,12]. Warner proposed a simplest definition of theranostic and it is “diagnostics plus therapy” [13]. It is assumed that the theranostic approach will not only improve the drug development and disease management but also will reduce the treatment risk and cost. During the past decade, various nanoparticles including iron oxide nanoparticles [14,15], carbon nanotubes [16], quantum dots (QDs) [17], gold nanoparticles [18,19], graphene [11,20] and silica nanoparticles [21,22] have been extensively studied for cancer theranostic. High surface energy and smaller particle size of nanoparticles result the aggregation and cellular toxicity, respectively which limit their clinical application [23,24]. In this context, over the last few years, carbon quantum dots (CQDs) have gained marvelous attention towards the scientist due to its exceptional water solubility, low toxicity, ease of synthesis and functionalization, exceptional photoluminescence (PL) and optical properties and large scale production with low cost.

The previous research works directed us to hypothesis the present work that the development of CQD based non-viral vector system could efficiently transit the gene of interest with high transfection efficiency and no toxicity to TNBC. Along with the therapeutic benefit if the vector could detect the presence of Cu(II) which in turn detect the stage of TNBC then it might be effective theranostic tool for TNBC.

To implement the hypotheses, we have prepared CD from a renewable source like sweet lemon peel and different generation of PAMAM dendrimers were conjugated with it and the synthesis was confirmed by transmission electron microscopy (TEM), UV–vis spectroscopy, fourier-transform infrared (FTIR) spectroscopy, X-ray Diffraction (XRD) analysis and fluorescence spectroscopy. Plasmid DNA (pDNA) was used to mimic the gene binding efficiency of our carrier system. Agarose gel electrophoresis assay was carried out to determine the gene binding efficiency. Cellular uptake study and *in vitro* transfection were performed in TNBC cell such as MDA-MB-231 cell. Selective detection of Cu(II) was carried out and intracellular fluorescence quenching in presence of Cu(II) was also evaluated in MDA-MB-231 cell.

2. Materials and methods

Ethylenediamine (EDA), Methylacrylate (MA) were purchased from Merck, India. 1-(3-Dimethylaminopropyl)-3-ethyl carbodiimide (EDC), N-hydroxysuccinimide (NHS), 4-morpholineethane sulphonic acid sodium salt buffer (MES), ethidium bromide, Triton X-100, thiazolyl blue tetrazolium bromide (MTT) were obtained from Sisco Research

Laboratories Pvt. Ltd., India. Dulbecco's Modified Eagle Medium (DMEM), Dulbecco's phosphate buffer saline (DPBS), trypsin, penicillin-streptomycin, fetal bovine serum (FBS), dimethyl sulphoxide (cell culture tested) and agarose were procured from Himedia, India. Polyethyleneimine (25 kDa), RGDS peptide, DAPI and paraformaldehyde were obtained from Sigma, Germany. DNase I kit was purchased from Thermo Scientific, India. pGL3 control vector (5.25 kb) having SV-40 promoter, was purchased from Promega (Madison, WI, USA). DH5-Alpha strain of *Escherichia coli* (E. coli) was used to propagate the plasmid and QIAGEN Midiprep DNA isolation Kit (USA) was used to isolate pDNA according to the manufacturer's instructions. pDNA concentration was determined from the absorbance at 260 nm and purity was also determined by spectrophotometry (A260/A280). pEGFP-N1 plasmid DNA (4.7 kb containing SV-40 promoter) and PGL3 plasmid DNA (5.25 kb, containing SV-40 promoter) were used as model gene. All other reagents used for carrying out the experiment, were analytical grade.

2.1. Synthesis of carbon quantum dot (CD)

Hydrothermal carbonization process was employed to synthesize CD from sweet lemon peel according to previous report [25] with slight modification. Briefly, sweet lemon peels were collected from local juice shop in Kolkata, India. Subsequently, peels were washed several times under running water followed by drying in hot air oven at 40 °C. The dried peels were cut into small pieces and 8 g of the small pieces were taken into 100 ml Teflon lined hydrothermal reactor containing 30 ml distilled water and kept the vessel in an oven under 180 °C for 3 h. After that, the hydrothermal reactor was allowed to cool to room temperature and the brown colored CD solution was filtered and concentrated through rotary evaporator (Model: Hei-VAP Advantage, Heidolph, Germany) followed by lyophilization (Model: 110N, Hahntech, South Korea) to get brown colored hygroscopic CD powder.

2.2. Synthesis of PAMAM dendrimer

PAMAM dendrimer was synthesized according to our previous report [26]. Amine terminated full generation PAMAM dendrimers (G1, G2 and G3) were synthesized by divergent technique starting from ethylenediamine (EDA) as core molecule followed by repeated Michael type addition and amidation reaction.

2.3. Synthesis of CD-PAMAM (CDP) conjugate

Full generation PAMAM dendrimers (G1, G2 and G3) were conjugated with CD by carbodiimide coupling reaction. Briefly, 0.2 g of powdered CD was dissolved in 5 ml of 10 mM MES buffer (pH 6.5). Excess EDC and NHS (an equimolar amount to each other) were added to the CD with constant stirring and continued for 1 h at room temperature to activate the carboxylic acid group of CD. Then 2 g of PAMAM dendrimer dissolved in 2 ml of 10 mM MES buffer solution was added slowly to the activated CD solution with stirring condition. After 16 h of reaction at room temperature, the solution was purified by dialysis using 3.5 kDa dialysis membrane (Snakeskin dialysis tubing, Thermo Fisher Scientific) against double distilled water for 3 days with change of water periodically followed by lyophilization to get different CDP conjugates such as CDP1, CDP2 and CDP3.

2.4. RGDS (Arg-Gly-Asp-Ser) decoration

50 mg CDP3 was weighted and dissolved in 5 ml of 10 mM MES buffer. 2 ml of 10 µg/ml RGDS solution was added into the CDP3 solution. Excess of EDC and NHS (equimolar to each other) were added to the above solution mixture and stirred at room temperature for 16 h. After that, the solution was dialyzed against double distilled water using 3.5 kDa dialysis membrane for 3 days with occasional change of

water followed by lyophilization for 3 days to get powdered RGDS decorated CDP3 (CDP3-RGDS).

2.5. Characterization

UV–Vis spectra of CD and CD-PAMAM conjugates (CDP1, CDP2 and CDP3) were recorded with Perkin Elmer Lambda 25 spectrophotometer within the range of 200–800 nm. The fluorescence spectra of CD and CDP conjugates were determined by fluoro-spectrophotometer (Perkin Elmer LS 55). The synthesis of CD and CDP conjugates were also characterized by FTIR spectroscopy (Perkin Elmer Spectrum 100 FTIR). All spectra were carried out within the frequency range of 4000–600 cm^{-1} with a scan rate of 8 consecutive scans at 1 cm^{-1} resolution. The crystal structure of samples was analyzed by an X-ray diffractometer (Panalytical, X'Pert) with Cu radiation ($\lambda = 0.154 \text{ nm}$) at 40 kV and 40 mA. Transmission electron microscopy (TEM) was carried out after depositing of CD or CDP aqueous solution on a carbon coated Cu grid and subsequently the images were taken by JEM-2100F (JEOL, Japan) operating at 200 kV. Zeta potential of CD and CDP was measured using Zetasizer Nano ZS, Malvern Panalytical Ltd, UK.

2.6. DNA complexation assay

CD or functionalized CDs/pDNA complexes were prepared by self-assembled complex coacervation technique according to our previous report [26–29] with slight modification. Briefly, predetermined amount of CD or CDPs and pDNA diluted in molecular biology grade water (Himedia, India) were taken in 0.5 ml of centrifuge tube separately. Equal volume of CD or functionalized CDs solution and pDNA solution were mixed at different weight ratios of 0.05, 0.1, 0.2, 0.5, 1.0 and 5.0 keeping pDNA amount constant at 0.5 μg in each weight ratio. The solution mixtures were vortexed immediately for 15–20 s and incubated at room temperature for 30 min to allow the formation of CD or CDPs/pDNA complexes.

The complexation capability of CD or CDPs with pDNA was confirmed by agarose gel electrophoresis assay. Freshly prepared CD or CDPs/pDNA complexes at different weight ratios were loaded in 0.8% agarose gel prepared in TAE buffer (40 mM tris-acetate and 1 mM EDTA solution) containing ethidium bromide (10 mg/ml) as DNA visualizer. Only pDNA was used as control. The gel was run at 100 V for 40 min using Consort power supply (Model: EV2650, Cleaver Scientific, UK) and subsequently the gel images were captured using Biotop gel documentation (FluorShot EVO SC750, China) system.

2.7. Cell culture

MDA-MB-231 (human epithelial breast cancer cell) cell was purchased from NCCS Pune, India and used for all *in vitro* studies including cytotoxicity assay, gene transfection efficiency and intracellular Cu(II) ion detection. The cells were cultured in DMEM medium containing 10% (v/v) FBS, 1% penicillin–streptomycin and 1% of 2 mM L-glutamine at 37 °C and CO_2 incubator (CelCulture, ESCO, Singapore) maintained at 5% CO_2 and 95% humidity according to supplier protocol.

2.8. Cell viability assay

Cell viability of CD and CDP conjugates (CDP1, CDP2, CDP3) was assessed against MDA-MB-231 cell according to our previous study [29]. Briefly, 5×10^3 cells per well were seeded in 96 well plate and incubated for 24 h at 37 °C in CO_2 incubator. The media of each well was replaced with fresh media containing predetermined concentration of CD, CDP1, CDP2, CDP3 (10, 25, 50, 100, 200 and 500 $\mu\text{g}/\text{ml}$) in respective wells. PEI, 25 kDa and untreated cell were used as positive and negative control, respectively. After 24 h of incubation at 37 °C, the media of each wells was discarded followed by washing with DPBS twice and then 100 μl of media containing MTT was added at a

concentration of 500 $\mu\text{g}/\text{ml}$ and incubated for another 4 h at 37 °C in CO_2 incubator. Thereafter, media was again removed carefully and 100 μl DMSO was added in each well to dissolve the formazan crystal. After further incubation for 15 min in dark, the absorbance was measured at 570 nm by multi-well Elisa reader (ErbaLisaScan EM, Transasia, India). The study was carried out in triplicate for each concentration. The cell viability (%) was calculated according to the following equation:

$$\text{Cell viability (\%)} = \frac{OD_{570}(\text{Sample})}{OD_{570}(\text{Control})} \times 100$$

where, $OD_{570}(\text{Sample})$ and $OD_{570}(\text{Control})$ are the absorbance of sample and control, respectively at 570 nm.

2.9. Blood compatibility assay

Blood sample was collected from healthy human male adults (25–31 years old). After discarding the plasma through centrifugation, the diluted red blood cells in PBS solution (200 μl) was added to variable concentration of CD, CDP3 and PAMAM G3 ranging from 10 to 200 $\mu\text{g}/\text{ml}$ and rest of the volume was made up to 1 ml with sterile PBS (pH = 7.4). Triton X-100 solution (1%, v/v) and PBS solution were used as positive and negative controls, respectively. After the incubation for 90 min at 37 °C, each of the tested solutions was centrifuged for 10 min at 2000 rpm. 200 μl of the supernatant was collected from each tube and put in separate wells of 96 wells plate. ELISA micro plate reader (Multiskan EX, LabSystems, Helsinki, Finland) was used to record the absorbance at a wavelength of 543 nm. The % hemolysis was calculated using the following equation:

$$\% \text{ Hemolysis} = \left(\frac{Abs_s - Abs_p}{Abs_n - Abs_p} \right) \times 100$$

where, Abs_s , Abs_n and Abs_p are the absorbance of sample, negative and positive controls; respectively.

2.10. DNase I enzymatic assay

Whether the carrier system could protect the gene of interest or not, we evaluated by DNase I assay where DNase I was used as a model enzyme. CDP3/pDNA complexes were freshly prepared at the weight ratios of 0.05, 0.1, 0.2, 0.5, 1.0 and 5.0. After that DNase I (1 unit/1 g of DNA) along with phosphate buffered saline (PBS) containing 5 mM MgCl_2 were added to the CDP3/pDNA complexes and incubated at 37 °C for 10 min followed by addition of 0.5 M EDTA to inactivate the DNase I activity. Only pDNA was used negative control. The digestion of naked pDNA and CDP3/pDNA complexes were analyzed by 0.8% agarose gel electrophoresis.

2.11. Cellular uptake study

Cellular uptake of CDP3 and CDP3-RGDS were carried out in 24 well plates. 500 μl of complete DMEM media containing 1×10^5 cells were seeded on to sterile glass cover slips placed in each well and incubated at 37 °C in CO_2 incubator. After 24 h of incubation, media was replaced with CDP3 or CDP3-RGDS containing complete media having concentration of 2 mg/ml after washing with DPBS twice and incubated for 4 h at 37 °C in CO_2 incubator. Thereafter, the media was removed and washed with DPBS three times to remove any attached CDP3 or CDP3-RGDS followed by addition of 4% paraformaldehyde to fix the cells. The cover slips were gently removed using hooked needle and mounted on clean glass slides by inverting the cover slip using glycerol as mounting media and finally sealed the cover slip using colorless nail polish. Confocal microscopic images were taken using confocal laser scanning microscope (CLSM, Olympus FV3000) at excitation wavelengths of 405, 473 and 559 nm.

2.12. *In vitro* transfection study

The transfection efficiency of functionalized CD (CDP3-RGDS) was carried out in MDA-MB-231 cells. Prior to the transfection, the cells were seeded in a 24 well plate at a density of 1×10^5 cells per well and cultured until 70–80% confluency was reached. After that, pDNA complexed with CDP3-RGDS in complete media at the weight ratios of 5, 10 and 20 containing 1 μ g of enhanced green fluorescence protein (EGFP) encoding pDNA in each ratios were added to pre-determined wells. After 4 h of post transfection, the cells were washed with DPBS twice followed by the addition of complete media and incubated for another 20 h at 37 °C in CO₂ incubator maintained at 5% CO₂ and 95% humidity. Thereafter, the media was discarded and the cells were fixed with 4% paraformaldehyde after washing with DPBS followed by nucleus staining with DAPI. The transfection efficiency was confirmed by CLSM after mounting the cover slip on glass slide.

2.13. Detection of Cu(II) and its selectivity

The Cu(II) ion detection assay was carried out by evaluating the fluorescence quenching of CD and CDP3 in presence of Cu(II) ion at different concentrations. In brief, 200 μ l of 10 mg/ml of CD or CDP3 aqueous stock solution was taken in a 2.0 ml tube followed by addition of Cu(II) solutions (here copper sulphate and chloride solutions were used) at different concentrations ranging from 0 to 2 mM diluted up to 2.0 ml using Britton-Robinson buffer (BR buffer) having pH of 7.0. Subsequently, the fluorescence spectra were recorded by fluorescence spectrophotometer. The selectivity for Cu(II) ion detection was evaluated in a similar manner with other ions such as Ag⁺, K⁺, Na⁺, Ca²⁺, Cd²⁺, Co²⁺, Fe²⁺, Mg²⁺, Mn²⁺, Zn²⁺, Al³⁺, Ni³⁺ and Fe³⁺ using the same concentration range.

2.14. Detection of Cu(II) in MDA-MB-231 cell

Intracellular Cu(II) ion detection was performed in MDA-MB-231 cell. After harvesting the cell, 1×10^6 cells per wells were seeded in a 24 well plate containing sterile glass cover slip and cultured for overnight at 37 °C in CO₂ incubator maintained at 5% CO₂ and 95% humidity. After 70–80% of confluency, media was replaced with fresh complete media containing 50 μ g of CDP3 and incubated for 4 h. After that, the media was removed followed by washing with sterile DPBS and again fresh media containing Cu(II) ions at predetermined concentration (0.0, 0.2, 1.0 and 2 mM) were added. After incubation for further 30 min, media was discarded and 4% paraformaldehyde solution was added after washing with DPBS and incubated for 20 min at 37 °C. No additional staining agents were used further. The intracellular fluorescence quenching of CDP3 in presence of Cu(II) ions was investigated under CLSM. All studies were carried out in triplicate.

2.15. Statistical analysis

All the experiments were carried out in triplicate for reproducibility and the data are presented here in the form of average value \pm the standard deviation. Two-way ANOVA was used for statistical analysis and *, **, *** and **** were considered for p values < 0.05, < 0.01, < 0.001 and < 0.0001, respectively.

3. Results and discussion

3.1. Synthesis of CD and CD-PAMAM conjugates

Here we developed CD based highly sensitive and selective biosensor for the detection of Cu(II) ion through conjugation of amine terminated full generation PAMAM dendrimer with CD. The synthesis of CD from sweet lemon peel waste followed by conjugation of PAMAM dendrimer of different generations (G1, G2 and G3) was confirmed by

FTIR and XRD analysis as shown in Figs. S1 and S2. Fig. S1 shows the FTIR spectra of CD, CDP1, CDP2 and CDP3. The broad peak at 3400 cm⁻¹ region and 2934 cm⁻¹ contributes the stretching of O–H and C–H bonds, respectively. A characteristic peak of CD is observed at 1715 cm⁻¹ which is corresponding to the stretching of C = O bonds present in –COOH group and it signifies the presence of carboxylic acid group in CD. But after conjugation of PAMAM dendrimer with CD through carbodiimide coupling agent, the peak for –COOH group disappears and new peaks appear at 1645 and 3289 cm⁻¹ which corresponds to the presence of amide and primary amine groups, respectively. Similar results were observed in the previous report [30] which suggests the synthesis of CDP conjugates.

The XRD spectra further confirms the synthesis of CD and CDP conjugates as shown in Fig. S2. A characteristic peak for (0 0 2) plane of CD is observed at 20.9° having d spacing of 4.2 Å which perfectly correlates with the previous reports [31–33]. The XRD spectra of CD demonstrates the amorphous nature compared to more crystalline bulk graphite which has comparatively less d spacing of 3.3 Å [32]. After conjugation of PAMAM dendrimer of G1 with CD, the peak was slightly shifted from 20.9° to 23.5° with decreasing the peak intensity of CD in CDP1. The result demonstrates the conjugation of PAMAM dendrimer of G1 occurs on the CD surface and consequently separates interlayer spacing of CDP1 which results the decreasing of peak intensity. With increasing the generation of PAMAM dendrimer from G1 to G3, the peak intensity gradually increases which may be attributed to the close packing of CDP interlayers through hydrogen bonding offered by the primary amine groups of PAMAM dendrimer. Therefore, the XRD spectra of CDP also confirms the successful synthesis of CDP conjugates. Fig. 1

The synthesis of CD and CDP was further supported by UV–vis and fluorescence spectroscopy as shown in Fig. 2. Fig. 2a shows the typical UV spectra of CD and CDPs. Typical characteristic peak of CD is obtained at 277 nm which corresponds to the π - π^* electronic transition of conjugated aromatic sp² hybridized C=C bonds present in graphitic core whereas the broad shoulder at ~330 nm is associated with n- π^* transition of C=O bond presents in –COOH group [28,34]. In addition to this, the extended tail of CD spectra in the visible range may be obtained through Mie scattering which ascribes the presence of carbon quantum dots [35]. After conjugation of PAMAM dendrimers with CD, the λ_{max} slightly shifted toward higher value after conjugation of PAMAM dendrimers. The decrease in absorption intensity after PAMAM dendrimer conjugation with CD may be attributed to the planarity loss of sp² hybridized graphitic core due to steric interaction offered by the conjugated PAMAM dendrimer and consequently the intensity gradually decreases with increasing dendrimer generation. The result further suggests the successful synthesis of CD and CDP conjugates.

When the CD was excited with different excitation wavelengths ranging from 260 to 380 nm, an excitation dependent fluorescence emission was obtained as shown in Fig. 2b. From Fig. 2b, it is found that the intensity of fluorescence emission peak increases with increase in excitation wavelength and maximum fluorescence intensity was obtained at the excitation wavelength of 340 nm. With further augmentation of excitation wavelength, the fluorescence emission peak intensity gradually decreased and red-shifted due to presence of various particles size of CDs and various functional groups at the surface of CD. This result is well agreement with the previous studies [36,37]. After conjugation of PAMAM dendrimers with CD, similar excitation dependent fluorescence emission was observed but the maximum emission fluorescence intensity at the corresponding excitation wavelength was changed as obtained in CD only. CDP1, CDP2 and CDP3 showed highest fluorescence emission peak at the excitation wavelengths of 400 nm, 380 nm and 420 nm, respectively.

The particle size and its morphology were determined by high-resolution transmission electron microscopy (HRTEM) and the respective images are shown in Fig. 3. Fig. 3a and c represent the HRTEM images of CD and CDP3, respectively. It is observed that CDs are spherical in

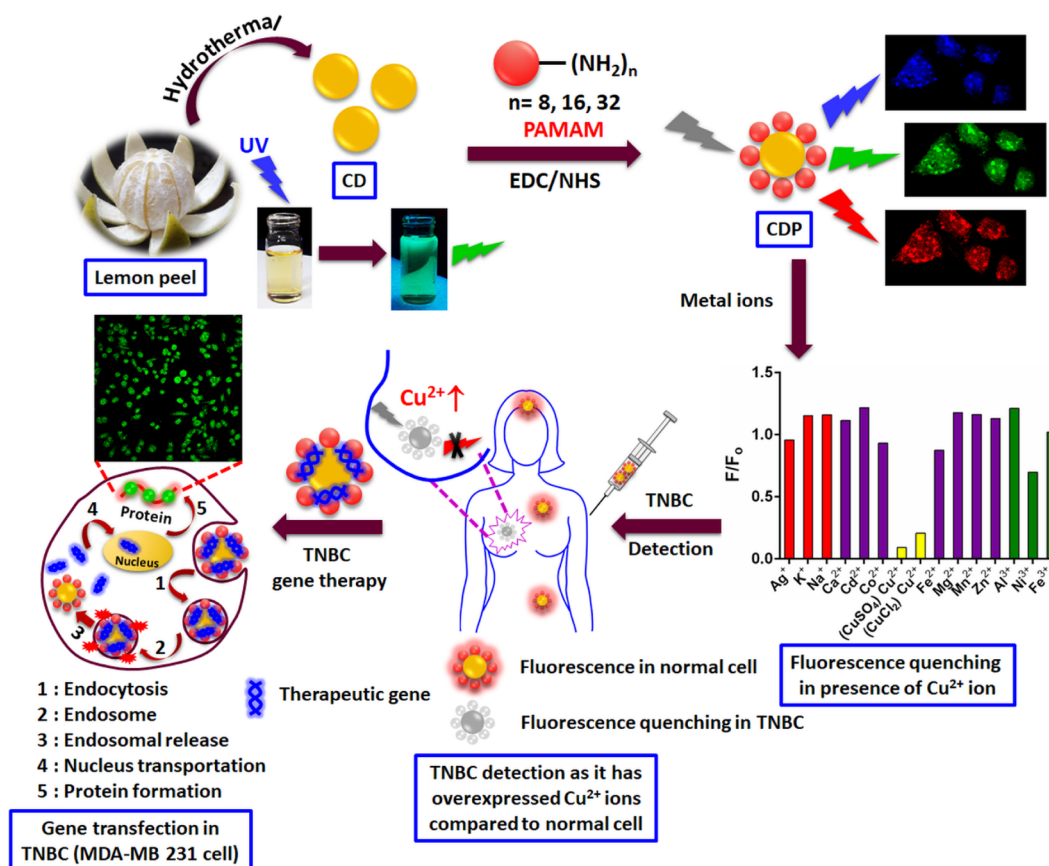


Fig. 1. Schematically representation of CD and CDPs and theranostics of TNBC.

shape and the particle size distribution range is from 1.5 to 6.5 nm as shown in Fig. 3b. As the PAMAM dendrimer was conjugated with the surface functional group (carboxylic acid group) of CD, it is expected the overall size of functionalized CD would increase slightly. Fig. 3c and d show the HRTEM image of CDP3 and its size distribution curve, respectively and it is found that the size of CD slightly increased after conjugation of PAMAM dendrimer and the size distribution of CDP3 has become from 7 to 27 nm as shown in Fig. 3d. The HRTEM images further support the conjugation of PAMAM dendrimer at the surface of CDs.

We further measured the surface zeta potential of CD and functionalized CDs. Fig. 3e shows the zeta potential of CD and CDPs. CD shows the negative zeta potential having the value of -3.5 ± 1.0 mV which also correlates with previous report [38]. The negative zeta potential arises due to the presence of carboxylic acid ($-\text{COOH}$) groups on the surface of CD. After conjugation of PAMAM dendrimers, the zeta potential of CD changes to positive and the magnitude of positive zeta potential gradually increases with increase in the generation of PAMAM dendrimers. The respective zeta potentials of CDP1, CDP2 and CDP3 are 1.1 ± 0.7 , 9.8 ± 0.1 and 12.8 ± 0.6 mV, respectively. The phenomenon is explained by the fact that the number of primary amine groups increases with increase in the generation of PAMAM dendrimer and consequently results the increment of zeta potential from CDP1 to CDP3. The positive zeta potential would be beneficial for the complexation with negatively charged gene or DNA through electrostatic interaction for gene delivery.

3.2. DNA complexation capability

After conjugation of PAMAM dendrimer with CD, we carried out agarose gel electrophoresis assay to confirm the gene complexation

capability of functionalized CD according to our previous reports [27,29]. Here pDNA was used as model gene and the corresponding gene complexation capability of CD and CDPs are shown in Fig. 4(a–d). Any cationic polymer can form complex with pDNA through electrostatic interaction between the positively charged polymer and negatively charged pDNA [39]. As CD possesses negative zeta potential as shown in Fig. 3e, it could not bind any pDNA at any weight ratios from 0.05 to 5.0 wt ratios (CD to pDNA weight ratio) as shown in Fig. 4a. But after conjugation of PAMAM dendrimer with CD, CDP starts to bind with pDNA although the pDNA complexation capability was dependent on the generation of PAMAM dendrimers. Fig. 4b, c and d show the pDNA complexation capability of CDP1, CDP2 and CDP3, respectively. From Fig. 4b–d, it is observed that CDP1 was able to complex completely all pDNA at CDP/pDNA weight ratio of 5.0, whereas CDP2 and CDP3 complexed all pDNA at the weight ratio of 1.0 and 0.5, respectively where the electrophoretic mobility of pDNA was completely retarded and all pDNA was retained at the loading site of the lane through the complex formation with CDP. The fact is well correlated with the zeta potential of CDPs. As the number of primary amine groups at the surface of PAMAM dendrimers increases with increase in PAMAM generation, consequently the surface positive zeta potential of CDPs also increases as shown in Fig. 3e and as a result the DNA complexation capability was also increased from CDP1 to CDP3 through strong electrostatic interaction between positively charged CDP and negatively charged pDNA. After functionalization of CDP3 with RGDS peptide, the gene complexation capability of CDP3-RGDS was further carried out and the corresponding agarose gel electrophoresis image is shown in Fig. S3. It is observed that the DNA complexation capability of CDP3 slightly decreased after modification of CDP3 with RGDS. CDP3 completely complexed with all pDNA at the weight ratio of 0.5 (shown in Fig. 4d) whereas CDP3-RGDS complexed all pDNA at slightly higher

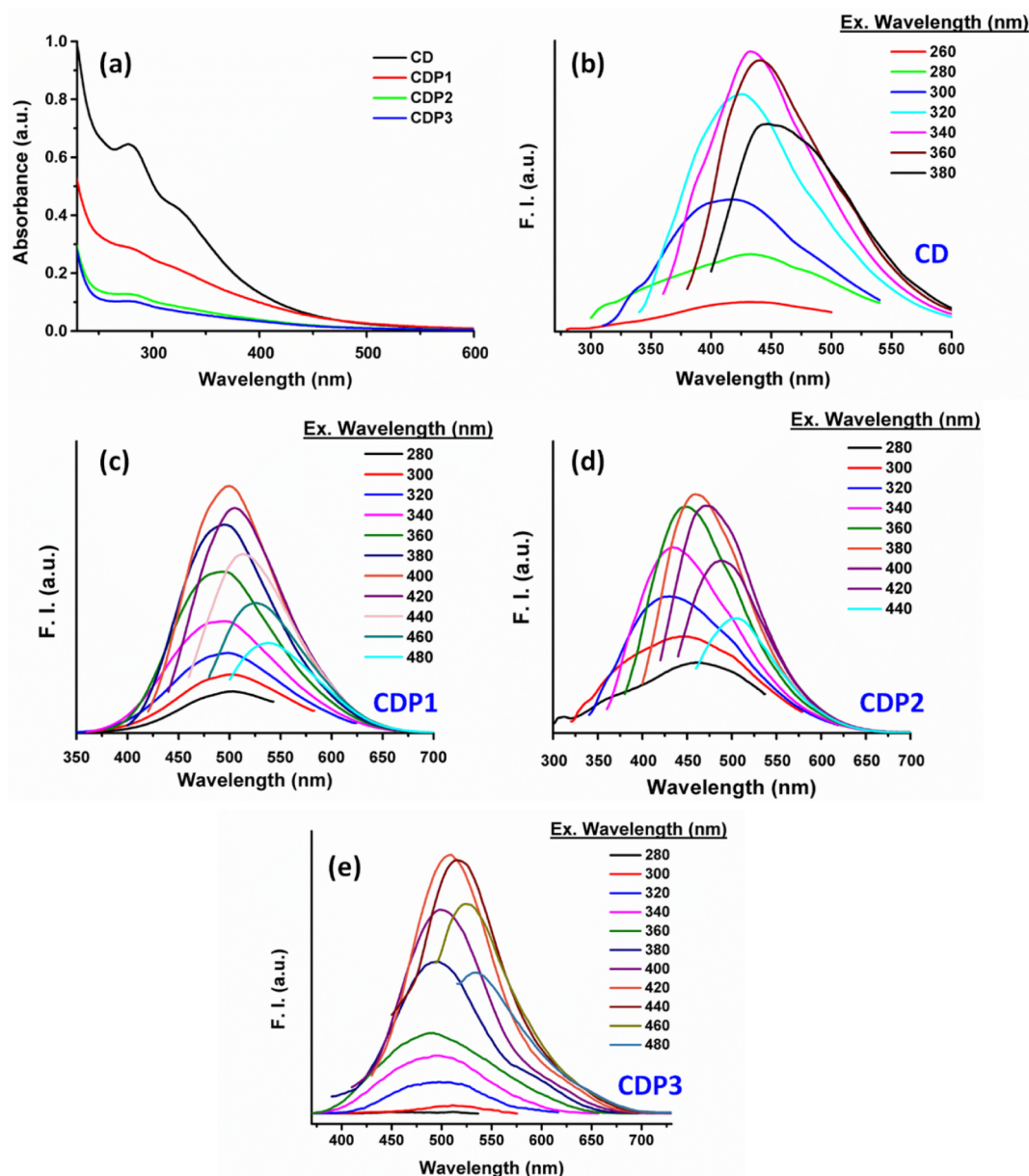


Fig. 2. UV spectra of CD, CDP1, CDP2, CDP3 (a) and Fluorescence spectra of CD (b), CDP1 (c), CDP2 (d) and CDP3 (e).

weight ratio of 1.0 (Shown in Fig. S4). This may be happened due to slight decrease of surface primary amine groups of CDP3 after conjugation of RGDS with CDP3 through carbodiimide coupling reaction.

The particle size and morphology of non-viral carrier/pDNA complexes are an important parameter for transfection efficiency in gene therapy application [40,41]. So, we checked the particle size and morphology of CDPs (CDP1, CDP2 and CDP3)/pDNA complexes at the weight ratio of 5.0 by HRTEM as shown in Figs. 4e and S4. It is observed that the size of CDP/pDNA complexes gradually increases with increase in the PAMAM generation. All CDPs formed spherical shaped complexes with pDNA and the average sizes of the CDP1/pDNA, CDP2/pDNA and CDP3/pDNA were around 3 nm, 7 nm and 9 nm, respectively (Figs. S4b, d and 4f). It is also noticed that the particle size of CDP3 (Fig. 3c and d) slightly decreased after complexation with pDNA. It may be happened because the surface free amine groups of CDP3 participated for complex formation with pDNA and as a result the surface positive charge of CDP3 was neutralized through negative charge of pDNA and resulted smaller size compared to uncomplexed CDP3.

3.3. *In vitro* toxicity of CD and CDPs

Before cellular studies it is necessary to check the *in vitro* toxicity of any unknown compound or carrier. So, we carried out the *in vitro* toxicity of CD and CDPs at various concentrations such as 10, 25, 50, 100, 200 and 500 $\mu\text{g}/\text{ml}$ on MDA-MB 231 cell by MTT assay as shown in Fig. 5a. From Fig. 5a, it is observed that CD did not show any toxicity up to the concentration of 200 $\mu\text{g}/\text{ml}$ where the cell viability remained above 100% but the cell viability significantly came down to $\sim 75\%$ at higher concentration (500 $\mu\text{g}/\text{ml}$). Similar dose dependent cell viability of carbon dots on MDA-MB-231 cell was obtained in previous study [42] where green tea derived carbon dots showed around 65% cell viability on MDA-MB-231 cell at a concentration of 270 $\mu\text{g}/\text{ml}$. After functionalization of CD with PAMAM dendrimer, the cell viability was slightly decreased compared to unmodified CD. Among the CDPs, CDP3 showed comparatively higher toxicity and the cell viability of CDP3 was $\sim 50\%$ at the concentration of 500 $\mu\text{g}/\text{ml}$. As PAMAM dendrimer of generation 3 possesses more primary amine groups compared to

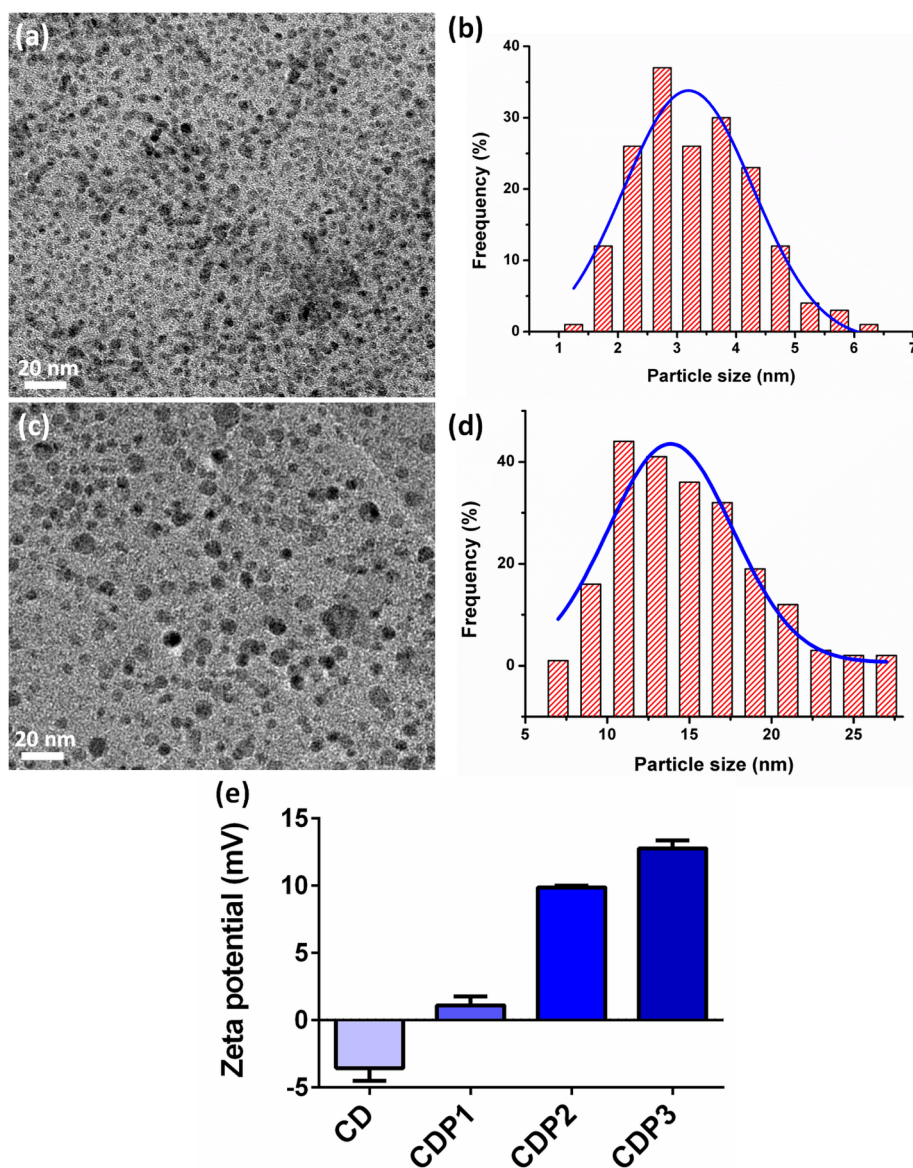


Fig. 3. TEM images of CD (a), CDP3 (c), their respective size distributions (b and d) and Zeta potential of CD, CDP1, CDP2 and CDP3 (e).

PAMAM-G1 and G2 and consequently it showed more toxicity through destabilizing of cell surface through ionic interaction between positive charge of primary amine groups and negative charge of cellular membrane [43,44]. Although, all CDPs showed significantly less toxicity compared to that of PEI, 25 kDa which is most widely used nonviral gene carrier [45]. Therefore, the functionalized CD is biocompatible and less toxic up to the concentration of 200 $\mu\text{g/ml}$.

3.4. *In vitro* hemolysis assay

Blood compatibility of any carrier system should be analyzed by *in vitro* hemolysis assay prior to the *in vivo* application to know that, is there any effect of the carrier on hemoglobin or not? The percent hemolysis of CD, CDP3 and PAMAM G3 at different concentrations of 10, 50, 100 and 200 $\mu\text{g/ml}$ were carried out and the corresponding results are shown in Fig. 5b and c. As the cell viability assay showed higher toxicity for CD and functionalized CD at the concentration of 500 $\mu\text{g/ml}$ (Fig. 5a), thus the hemolysis assay was carried out up to the concentration of 200 $\mu\text{g/ml}$. Triton X-100 (1%, v/v) and PBS (pH 7.4) were used as positive and negative control; respectively. Fig. 5b and c show the corresponding photographic images and bar graph of hemolysis

assay; respectively. From Fig. 5b and c, it is found that a negligible amount of hemolysis was observed with all tested compounds after 90 min of incubation compared to the positive control, Triton x-100. Both CD and CDP3 showed around 5% hemolysis at the concentration of 200 $\mu\text{g/ml}$. Although the hemolysis was concentration dependent and the percent hemolysis was gradually increased with increase in concentration for both CD and CDP3. CDP3 showed slightly more hemolysis at the concentration of 200 $\mu\text{g/ml}$ compared to CD only although there was no significant difference. The little higher amount of hemolytic effect of CDP3 may be attributed due to the conjugation of PAMAM G3 which itself showed higher hemolytic effect compared to CD. However, the percent of hemolysis of CDP3 was only around 5% even at higher concentration of 200 $\mu\text{g/ml}$, which is almost negligible to cause blood incompatibility. Therefore, CDP3 may be used safely in *in vivo* application.

3.5. DNase I assay

Enzymatic digestion of gene is a common phenomenon for poor transfection efficiency during the gene transfection using naked gene or in case of inefficient gene carrier [46,47]. An efficient gene carrier

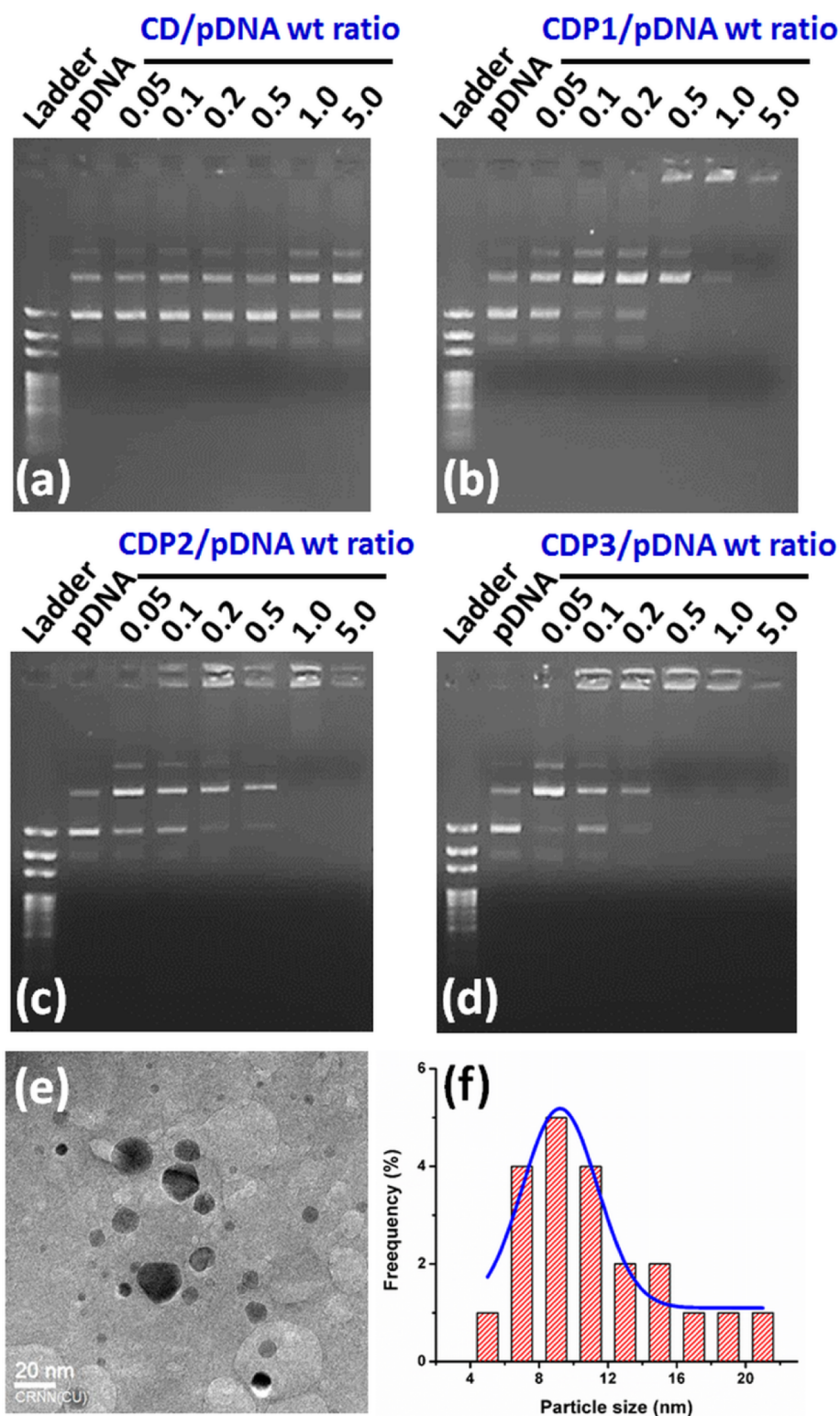


Fig. 4. Agarose gel electrophoresis assay of CD/pDNA (a), CDP1/pDNA (b), CDP2/pDNA (c) and CDP3/pDNA complex (d). The corresponding TEM image (e) and particle size distribution (f) of CDP3/pDNA complex.

should protect the gene from enzymatic digestion for successful gene therapy. To know the gene protection capability of the functionalized CD against enzymes, we carried out the DNase I assay of CDP3/pDNA complexes at various weight ratios where DNase I was used as a model enzyme as shown in Fig. 5d. DNase I showed its reactivity in lane 2 where it completely digested all pDNA and no pDNA band was found as it was seen in lane 1. From Fig. 5d, it is found that CDP3 could not

protect pDNA against DNase I digestion at the weight ratio of 0.05 (lane 3) and 0.1 (lane 4). However, in Fig. 4d it is observed that CDP3 started to form complex formation with pDNA from the weight ratio of 0.1, so, CDP3 should protect pDNA against the digestion of DNase I at that weight ratio, which is not happened. This phenomenon can be explained that CDP3 might not form tight complex with pDNA at the weight ratio of 0.1 (as electrophoretic mobility of some unbound pDNA

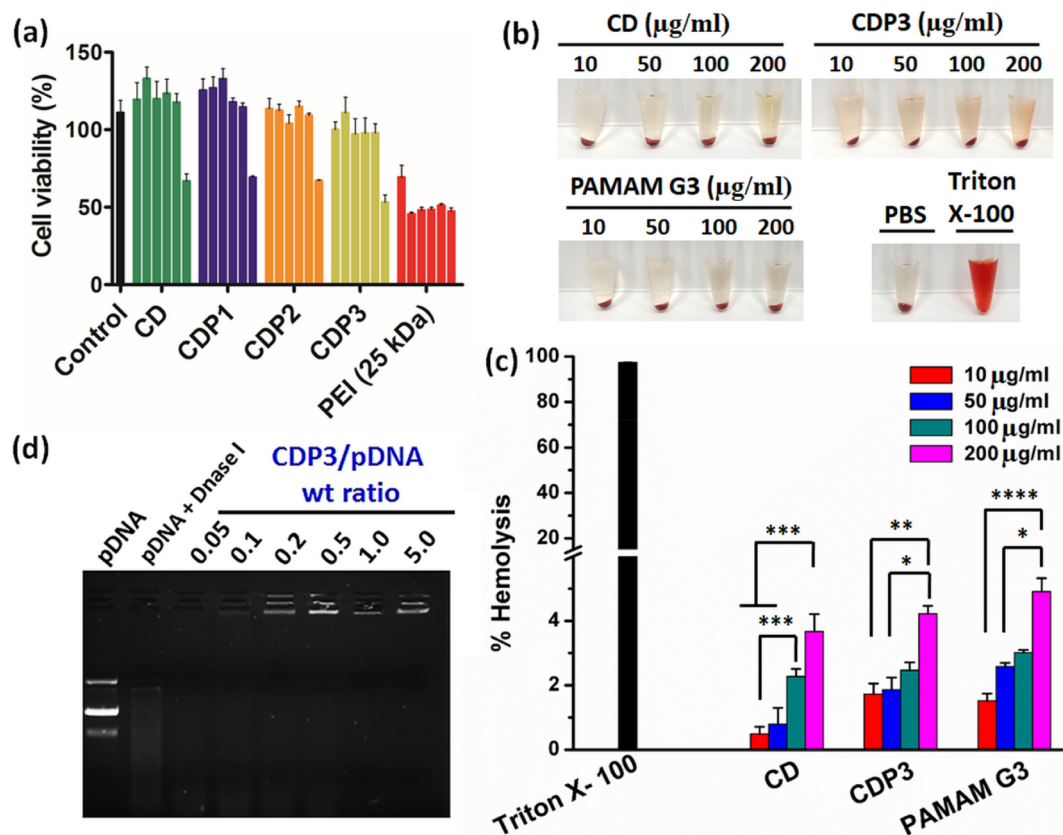


Fig. 5. Cell viability assay in MDA-MB-231 cell line at different concentrations such as 10, 25, 50, 100, 200 and 500 µg/ml (a), photographic images (b) and bar graph (c) of hemolysis assay, and DNase-I digestion assay (d).

was observed in Fig. 4d) and as a result complete pDNA digestion was occurred at that weight ratio. But with increasing the CDP3/pDNA weight ratio, it formed tight complex with pDNA due to increase in positive charge of CDP3 and consequently started to protect the pDNA efficiently against DNase I digestion from the weight ratio of 0.2 (lane 5, Fig. 5d). Similar observation was found in our previous report where cationic polymer protected the pDNA against DNase I digestion at higher polymer/pDNA weight ratio [48]. Therefore, the CDP3/pDNA complex beyond the weight ratio of 0.2 may be useful for successful gene delivery.

3.6. Cellular uptake

For efficient gene transfection efficiency, adequate cellular uptake of the carrier in any cell of interest is necessary. Poor cellular uptake is a major issue for the poor gene transfection efficiency by nonviral carrier [49,50]. Here we observed the cellular uptake of CDP3 at the concentration of 200 µg/ml in MDA-MB-231 and unfortunately we did not get promising cellular uptake (Fig. S5). Then, we further modified CDP3 through the conjugation of RGDS to enhance the cellular uptake. It is reported that MDA-MB-231 cancer cell possesses overexpression of RGD receptor $\alpha v \beta_3$ integrin [51]. After conjugation of RGDS with CDP3, the cellular uptake significantly increased at the concentration of 200 µg/ml as shown in Fig. 6. From Fig. 6 it is found that CDP3-RGDS was internalized into the cell and almost equally distributed into the cytoplasm of the cells. Interestingly, the functionalized CDP3 (CDP3-RGDS) showed fluorescence under three different excitation wavelengths i.e. 405 nm (blue fluorescence, Fig. 6a), 473 nm (green fluorescence, Fig. 6b) and 559 nm (red fluorescence, Fig. 6c) which further justify the excitation dependent emission of fluorescence of CDPs as obtained in Fig. 3c–e. As we did not use any staining agent to investigate the fact that whether the fluorescence of CDP3-RGDS at

different excitation wavelengths came from the same source or not, we co-localized the blue and red fluorescence images, which produced cyan color (Fig. 6d); the green and red fluorescence images produced yellow color (Fig. 6e) and red and blue fluorescence images produced pink color (Fig. 6f). To prove the phenomenon, we further drawn vertical and horizontal axes throughout a particular portion of the magnified images (Fig. 6g, h, and i) and the corresponding peaks for blue, green and red fluorescence almost merged each other for both horizontal (Fig. 6j) and vertical (Fig. 6k) axes which indicates that the blue, green and red fluorescence came from the same source i.e. from CDP3-RGDS. Therefore, the functionalized CDP (CDP3-RGDS) may be an attractive bio-imaging agent for TNBC cell imaging purpose.

3.7. In vitro transfection

Due to poor cellular uptake of CDP3 into the cell, we did not perform transfection efficiency with CDP3. CDP3-RGDS/pDNA (eGFP encoded pDNA) complexes at the weight ratios of 5, 10 and 20 were used for transfection efficiency in MDA-MB-231 cell and the corresponding transfection efficiency of CDP3-RGDS/pDNA at the weight ratio of 20 is shown in Fig. 7. From Fig. S3, it is found that CDP3-RGDS is able to form complex completely with pDNA from the weight ratio of 1.0 and therefore we used higher weight ratios (5, 10 and 20) for transfection study. Since the concentration of CDP3-RGDS (40 µg/ml) was less compared to the concentration used for cellular uptake study (200 µg/ml), hence the fluorescence signal (blue, green and red) from the CDP3-RGDS was extremely low. So, we used DAPI for nucleus staining of the cells. Fig. 7b shows good green fluorescence of the cells which is obtained due to green fluorescence protein produced through transfection of eGFP-pDNA by CDP3-RGDS. Blue fluorescence (Fig. 7a) is corresponding to the DAPI stained nucleus of the cells. As the functionalized CDP3 itself shows green fluorescence (as shown in Fig. 6b), it may

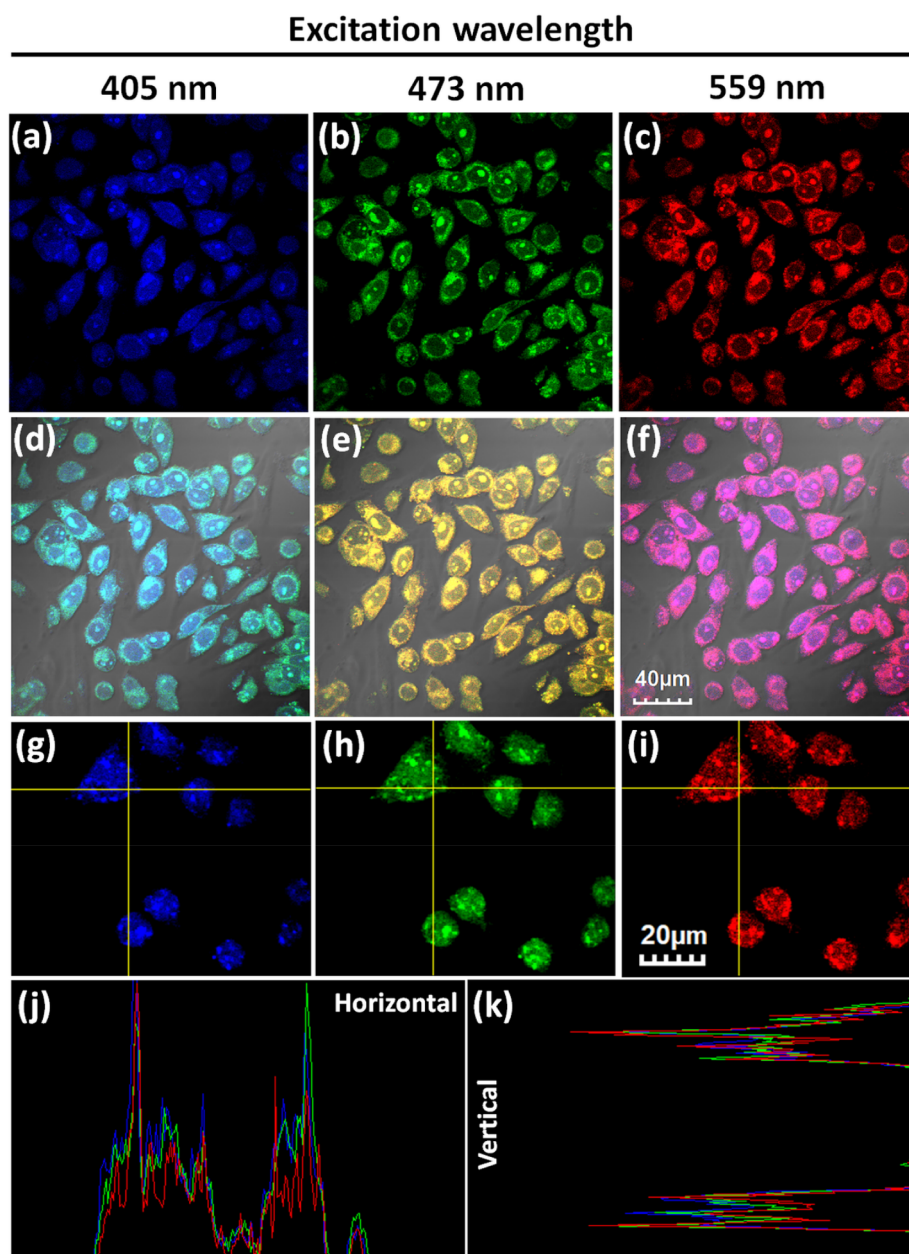


Fig. 6. Cellular uptake of CDP3-RGD in MDA-MB-231 cell and the corresponding confocal fluorescence microscopy image at the excitation wavelength of 405 nm (blue filter) (a), 473 nm (green filter) (b) and 559 nm (red filter) (c); Co-localization images of blue and green filter image (d), green and red filter image (e) and red and blue filter image (f); zoomed image of Fig a (g), Fig b (h) and Fig c (i); fluorescence intensity peaks obtained through horizontal line (j) and vertical line (k). (For interpretation of the references to color in this figure legend, the reader is referred to the web version of this article.)

conflict with the green fluorescence obtained from transfection of eGFP-pDNA by CDP3-RGDS. To overcome the confusion, we selected a particular region of Fig. 7a, b and c and drawn vertical and horizontal axes through the selected area (shown in Fig. 7d, e and f) to check whether the corresponding fluorescence peaks would merge each other or not as shown in Fig. 6j and k. Interestingly, it is found that the corresponding fluorescence peaks did not merge at all with each other. Apart from this, the peak intensity and its position were totally different from each other as shown in Fig. 7g (for horizontal axis) and h (for vertical axis). Therefore, it can be concluded that the fluorescence signals came from different sources i.e. blue, green and red fluorescence came from DAPI staining, green fluorescence protein through transfection and functionalized CD, respectively. We further carried out the co-localization of Fig. 7d, e and f and the corresponding co-localized images are shown in Fig. 7i (co-localization of Fig. 7d and e), j (co-localization of Fig. 7e and

f) and k (co-localization of Fig. 7d and f). It is observed that very few number of green dots co-localized with blue color and consequently resulted very few numbers of cyan colored dots (Fig. 7i, shown by yellow headed arrow). Similarly, very few numbers of green and red dots co-localized each other and as a result few numbers of yellow colored dots were observed (Fig. 7j, shown by white headed arrow) after co-localization. Therefore, it is confirmed that the green fluorescence was obtained due to the transfection of eGFP-pDNA by CDP3-RGDS and CDP3-RGDS may be used as efficient gene carrier to TNBC for gene therapy application.

3.8. Detection and selectivity of Cu(II) ion

As the Cu(II) ion concentration remains comparatively high in TNBC patients according to the recent clinical study [10], if CDP3 could

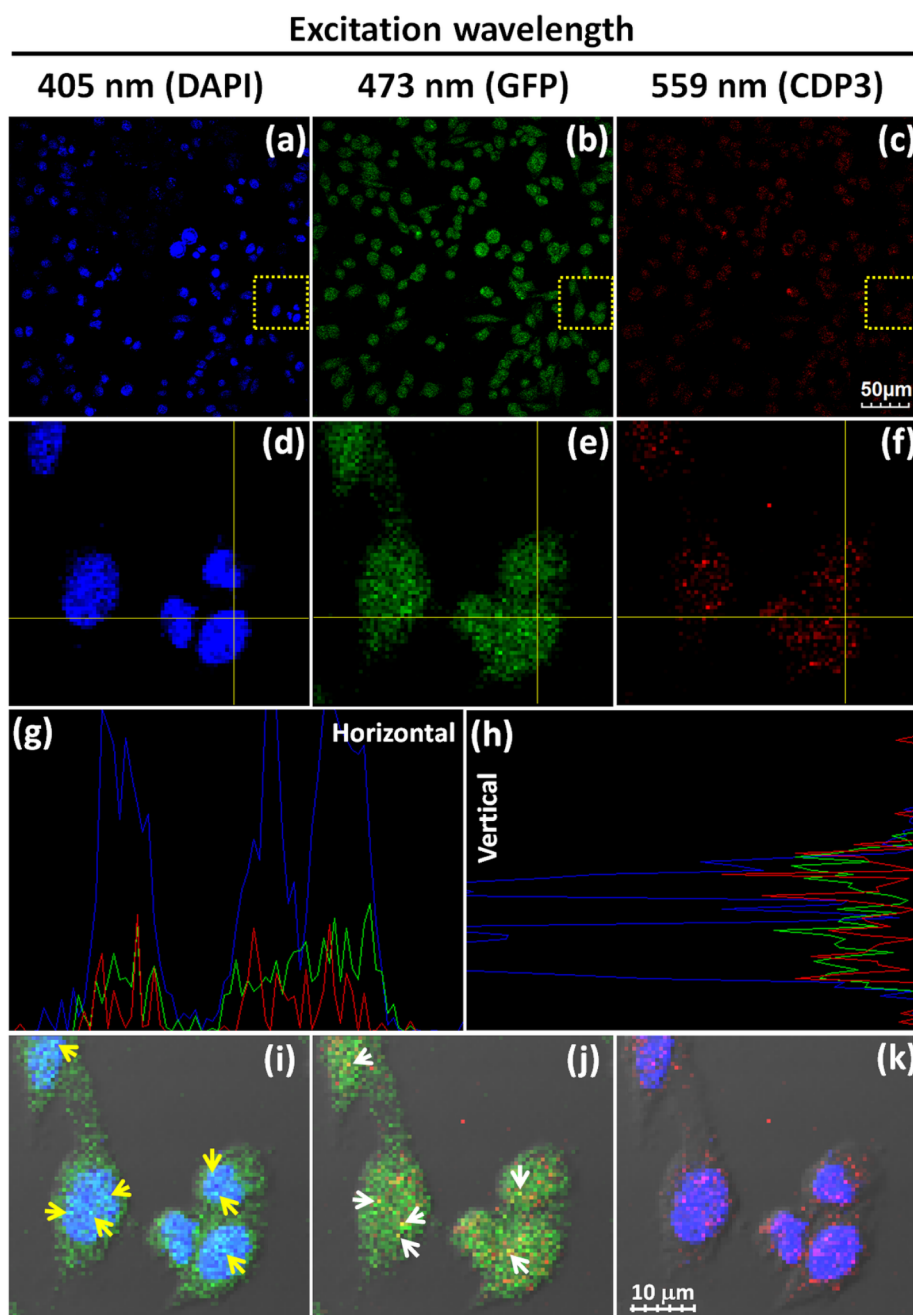


Fig. 7. *In vitro* transfection of CDP3-RGD in MDA-MB-231 cell and the corresponding confocal fluorescence microscopy image at the excitation wavelength of 405 nm (blue filter) (a), 473 nm (green filter) (b) and 559 nm (red filter); zoomed image of Fig a (d), Fig b (e) and Fig c (f); fluorescence intensity peaks obtained through horizontal line (g) and vertical line (h); Co-localization images of blue and green filter image (i), green and red filter image (j) and red and blue filter image (k). (For interpretation of the references to color in this figure legend, the reader is referred to the web version of this article.)

detect Cu(II) ion selectively and efficiently then CDP3 could be used as theranostics application for TNBC patient. Therefore, we carried out Cu (II) ion detection through measuring the fluorescence quenching of CD and CDP3 (fixed amount of CD or CDP3, 200 μ l of 10 mg/ml solution) in presence of copper sulphate as the source of Cu(II) ion at various concentrations (0, 0.01, 0.05, 0.10, 0.25, 0.50, 1.00, 1.50 and 2.00 mM) as shown in Fig. 8a and b. From Fig. 8a, it is observed that the fluorescence intensity of CD was gradually decreased with increase in the Cu (II) ion concentration and the fluorescence quenching efficiency of it became almost constant beyond the Cu(II) ion concentration of 0.1 mM as shown in Fig. 8c. In comparison, CDP3 showed significant fluorescence quenching in presence of Cu(II) ion and the fluorescence intensity of CDP3 drastically decreased with increase in the Cu(II) ion

concentration as shown in Fig. 8b. Fig. 8c shows that the fluorescence quenching efficiency of CDP3 was significantly increased with increasing the Cu(II) ion concentration and reached up to 93% at the Cu (II) ion concentration of 2.0 mM whereas unmodified CD showed only ~ 31% quenching efficiency at the same Cu(II) ion concentration (Fig. 8d). Till date several carbon dots have been developed for Cu(II) ion detection as summarized in Table 1. Among the reported CDs only graphene oxide derived CD showed highest fluorescence quenching efficiency having ~ 88% quenching efficiency. Although some other reported CDs such as citric acid and branched PEI derived CD [52] as well as lily bulb derived CD [36] also showed similar LOD of 0.01 μ M but both of them showed only ~ 77% and ~ 67% quenching efficiency, respectively which was much lower than that of CDP3. We further

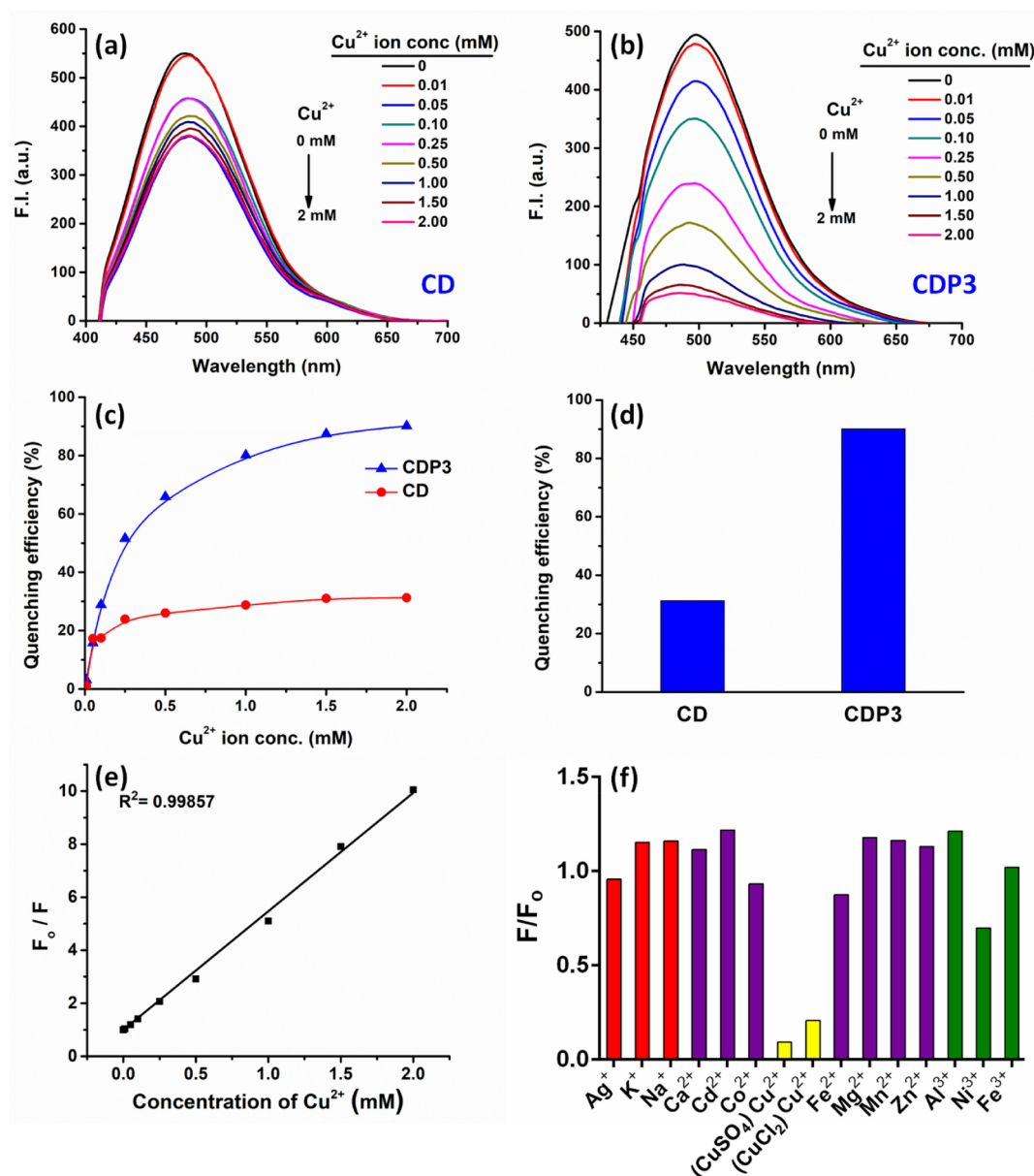


Fig. 8. Fluorescence quenching of CD in presence of different Cu(II) concentrations such as 0, 0.01, 0.05, 0.1, 0.25, 0.5, 1.0, 1.5 and 2.0 mM (a); Fluorescence quenching of CDP3 in presence of different Cu(II) concentration such as 0, 0.01, 0.05, 0.1, 0.25, 0.5, 1.0, 1.5 and 2.0 mM (b); comparative quenching efficiency of CD and CDP3 at the Cu(II) ion concentration of 0, 0.01, 0.05, 0.1, 0.25, 0.5, 1.0, 1.5 and 2.0 mM (c); bar plot of comparative quenching efficiency at the Cu(II) ion concentration of 2.0 mM (d); linear detection of Cu(II) ion concentration obtained by plotting of F_0/F vs concentration of Cu(II) ion (e) and response profile of fluorescence quenching of CDP3 in presence of different metal ions (f).

Table 1

Comparative representation of different CD based sensor for Cu(II) ion detection.

Components for designing CD based probe	Synthesis Technique	Limit of Cu^{2+} Detection (μM)	Quenching Efficiency (%)	References
D-glucose and ethane-1,2-diamine	Microwave	1.8	~50	[54]
Citric acid,L-cysteineand dextrin	Microwave	0.02	~84	[55]
Citric acid and branched poly(ethylenimine)	Pyrolysis	0.01	~77	[52]
Bamboo leaves	Hydrothermal	0.1	~60	[37]
Citric acid and ethylenediamine	Microwave	0.1	~63	[56]
Lemon juice and l-arginine	Thermal coupling	0.05	~82	[57]
Ethylenediamine and phosphorus pentoxide	Carbonization	10	~68	[58]
Lily bulbs	Microwaves	0.01	~67	[36]
Graphene oxide	Hydrothermal	0.2	~88	[59]
Sweet lemon peels and PAMAM	Hydrothermal	0.01	~93	Present work

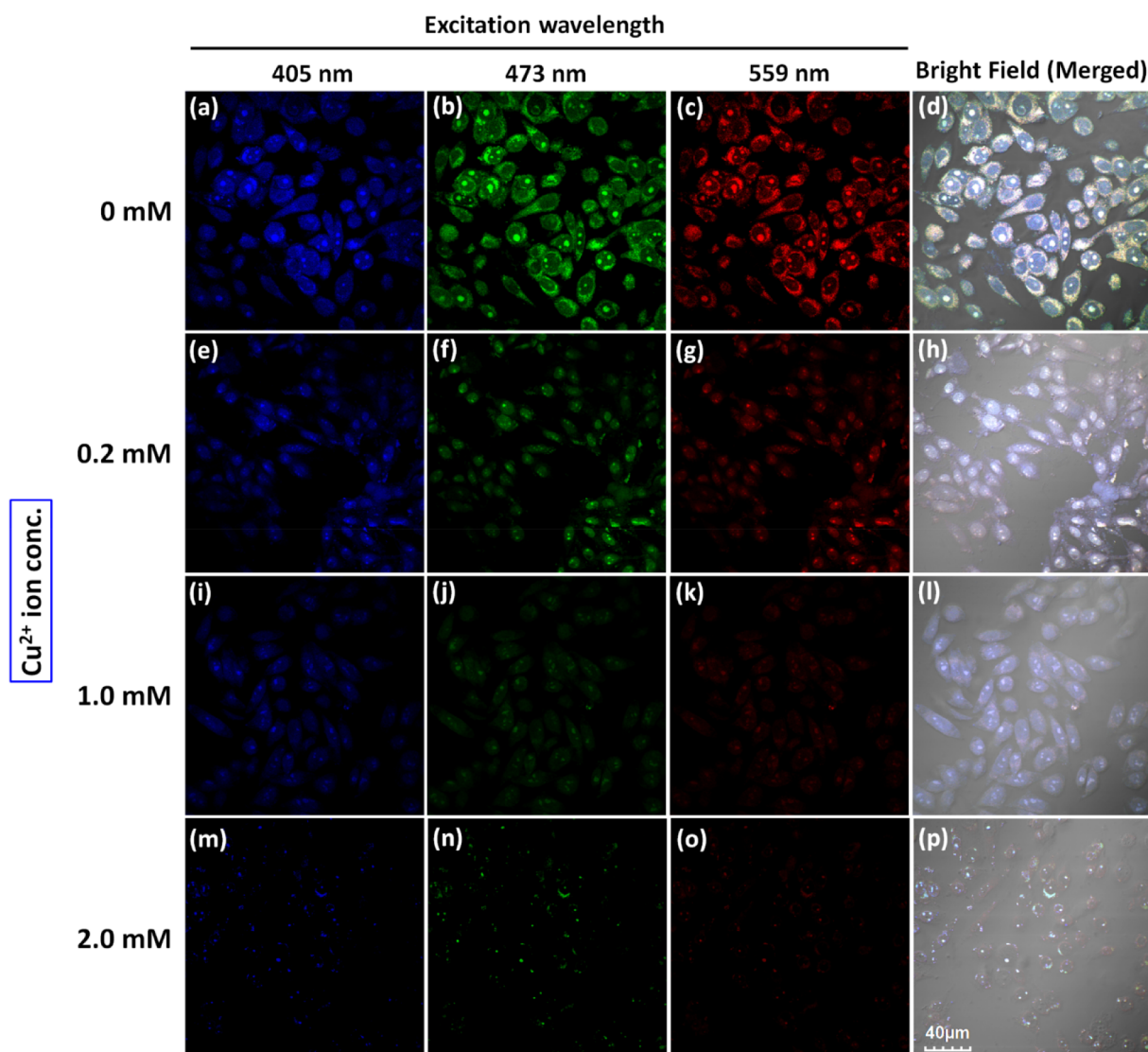


Fig. 9. Detection of cellular Cu(II) ions in MDA-MB-231 cell by CDP3 and the corresponding fluorescence images at the excitation wavelengths of 405, 473 and 559 nm and merged images at the Cu(II) ion concentration of 0 mM (a–d), 0.2 mM (e–h), 1.0 mM (i–l) and 2.0 mM (m–p).

calculated the linear range for Cu(II) ion detection as shown in Fig. 8e and CDP3 showed very large linear detection range of 0–2 mM with the regression coefficient value of 0.99857. In a recent clinical study [10], it is found that Cu(II) ion concentration increases in the serum of breast cancer female patient. Therefore, CDP3 may be an effective biosensor for breast cancer detection through Cu(II) ion sensing.

To further assess the selectivity towards Cu(II) ion, the fluorescence quenching of CDP3 was also investigated in presence of different cationic metal ions including Ag⁺, K⁺, Na⁺, Ca²⁺, Cd²⁺, Co²⁺, Cu²⁺, Fe²⁺, Mg²⁺, Mn²⁺, Zn²⁺, Al³⁺, Ni³⁺ and Fe³⁺ at the concentration of 2 mM and the corresponding fluorescence quenching is shown in Fig. 8f. It is observed from the Fig. 8f that the Cu(II) ion selectively and significantly quenched the fluorescence intensity of CDP3 where as other metal ions remained almost inactive. Here we also used different sources of Cu(II) ions i.e. CuSO₄ and CuCl₂ to check that is there any effect on fluorescence quenching or not? But both of them showed efficient fluorescence quenching of CDP3.

To investigate the superior quenching efficiency of CDP3, UV spectra of CDP3 and CD in presence of Cu(II) ion was analyzed and found the red-shift of CDP3 spectra in presence of higher concentration of Cu(II) ion along with the formation of a new broad absorption peak at around 500–700 nm (Fig. S6) compared to that of CD. To further

confirm the fact, absorption spectra of CDP3 in presence of different concentration of Cu(II) (0–2 mM) were also analyzed. From Fig. S7, it is found that the intensity of the absorption peak was gradually increased with increase in the concentration of Cu(II) ion. This phenomenon indicated the formation of a complex between Cu(II) and the abundant amino groups present on the surface of CDP3. The cupric amine mediated fluorescence quenching of CDs containing abundant amino groups was also justified by Dong et al. [52] and Wang et al. [53]. As unmodified CD doesn't have any amino functionality on their surface, they were not strongly quenched by the Cu(II) [52] in turn proves that the formation of cupric amine plays an important role in detection of Cu(II) ion selectively. Fig. S8 also shows the linear detection range of Cu(II) ion within 0–2 mM with the regression coefficient value of 0.9975.

Therefore, it is found that CDP3 would be an efficient biosensor for breast cancer through selectively detecting Cu(II) ion which remains abundant in breast cancer patient compared to normal patient.

3.9. Detection of Cu(II) in MDA-MB-231 cell

Metastases influence the rate of mortality and morbidity in patients affected by TNBC. In previous research works it has been found that bioavailable copper plays an important role not only in the process of

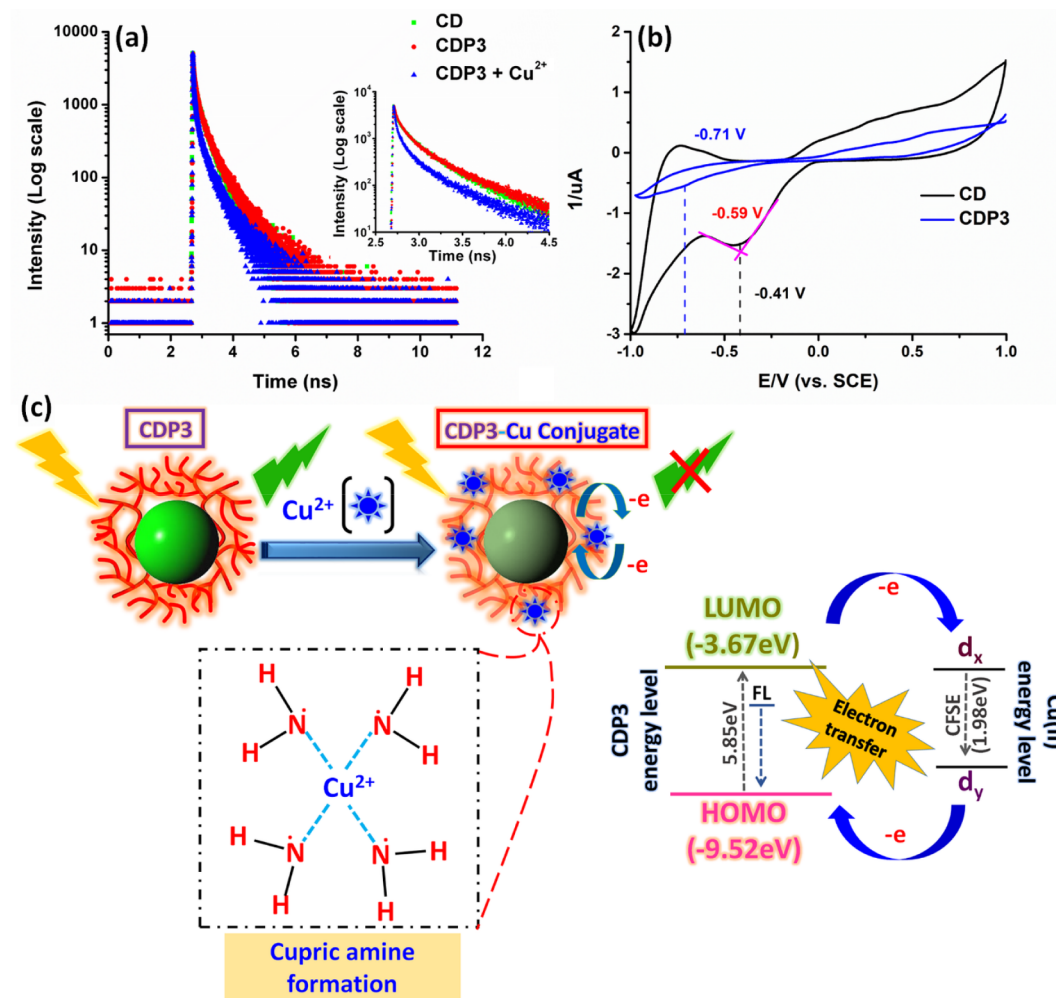


Fig. 10. Time-correlated single-photon counting analysis of CD, CDP3 and CDP3 + Cu(II) (a); cyclic voltametry spectra of CD and CDP3 (b); and schematic representation of quenching mechanism (c).

Table 2

Detailed analytical data of time correlated single photon counting spectra of CD, CDP3 and CDP3-Cu(II) complex.

Sample	Chi-square	τ_1 (ns)	τ_2 (ns)	τ_3 (ns)	Average $\tau_{1/2}$ (ns)
CD	1.025	1.784	5.802	0.256	1.25
CDP3	1.136	1.736	6.124	0.350	1.41
CDP3-Cu(II)	1.080	1.244	5.404	0.199	0.66

Table 3

Reduction potential (E_{Red}), energy band gap (E_g), E_{LUMO} and E_{HOMO} of CD and CDP3.

Sample	E_{Red} (eV)	E_{LUMO} (eV)	E_g (eV)	E_{HOMO} (eV)
CD	-0.41	-3.99	5.29	-9.28
CDP3	-0.71	-3.67	5.85	-9.52

metastases but also act as an essential factor in angiogenesis, tumor proliferation, growth and motility. Various pre-clinical studies have demonstrated that copper depletion, affect the growth as well as the other related condition of tumor metastases [60–63]. It has been also reported that in TNBC patients, among the other metal ions, copper elevated markedly [10]. So, the detection of copper ion would be a diagnostic approach in case of TNBC. However, presence of metal ion in

the biological system is an unique challenge to detect because bio-available metals, like copper, are present within the macromolecules [60]. Previous studies demonstrated the detection of Cu(II) in other cells like Hela, A549, HepG2, Hep-2 [53] whereas, in the present study we detect the Cu(II) ion by CDP3 in MDA-MB-231 cell and the corresponding confocal microscopy images are shown in Fig. 9. Fig. 9a–c show nice intense fluorescence of CDP3 in absence of Cu(II) ion under three excitation filters blue (Fig. 9a), green (Fig. 9b) and red filter (Fig. 9c). It is also observed that the nanodots of CDP3 were homogeneously distributed throughout the cytoplasm. But, the fluorescence intensity of CDP3 was gradually decreased with increase in the intracellular Cu(II) ion concentration from 0.2 to 1.0 to 2.0 mM (Fig. 9e–p). At the intracellular Cu(II) ion concentration of 2.0 mM, the fluorescence intensity of CDP3 was almost disappeared under all excitation filters (Fig. 9m, n and o). Therefore, CDP3 was not only selectively detected Cu(II) ion from solution but also efficiently detected Cu(II) ion intracellularly in TNBC cell. As the pH of the cancer tumor environment remains acidic i.e. pH 6 to pH 6.5 [64,65], so we also checked the effect of pH on fluorescence quenching of CDP3 in presence of Cu(II) ion. Fig. S9 shows the fluorescence quenching of CDP3 in presence of Cu(II) ion (2 mM) at pH 6 and 4. It is observed that the CDP3 showed around 70% quenching efficiency at pH 6 whereas only around 40% quenching efficiency was obtained at pH 4. This phenomenon may be explained by the fact that CDP3 got more protonation at lower pH i.e. pH 4 compared to that of pH 6 and resulted lower quenching efficiency. As the tumor microenvironment possesses the pH

within 6 to 6.5, therefore CDP3 may be suitable for the detection of TNBC effectively with nearly 70% quenching efficiency.

3.10. Fluorescence quenching mechanism

The fluorescence quenching are of two types such as static quenching and dynamic or collisional quenching. The static quenching happens when a non-fluorescent complex is formed between the quencher and the fluorophore and it can be described by Stern–Volmer equation [66] as follows:

$$\frac{F_0}{F} = 1 + k_{sv}[Q]$$

where, F_0 and F are the intensities of the fluorescence in absence and presence of quencher, respectively. k_{sv} is the association constant and Q is the concentration of the quencher present in the solution. The fluorescence lifetime of the component in absence or in presence of quencher remains same in case of static quenching.

On the other hand, dynamic or collisional quenching follows Stern–Volmer equation [66] which can be represented as follows:

$$\frac{F_0}{F} = \frac{\tau_0}{\tau} = 1 + k_q\tau_0[Q]$$

where, k_q is the rate constant of dynamic or collisional quenching. τ_0 and τ are the lifetime of the fluorescence of the component in absence and presence of quencher, respectively.

The mechanism of quenching could be attributed by electron transfer [67], inner filter effect [52] or aggregation induced emission quenching [68] etc. In present work the probable mechanism of quenching was determined by fluorescence lifetime and cyclic voltammetry study. To explain the fluorescence lifetime analysis, we have plotted Stern–Volmer equation to critically describe the Cu(II) ion concentration dependent fluorescence intensity of CDP3. Fig. 8e shows the Stern–Volmer analysis where F_0/F was plotted against Cu(II) ion concentration and a linear Stern–Volmer plot was found throughout the range of Cu(II) ion concentration taken for analysis i.e. 0–2 mM with the R^2 value of 0.99857. To further investigate the quenching process time-correlated single-photon counting (TCSPC) experiment was carried out in presence and absence of Cu(II) ion. Fig. 10a shows the fluorescence decay of CD, CDP3 and CDP3-Cu(II). From Table 2 and Fig. 10a, it is found that CD and CDP3 possessed almost similar lifetime with negligible shift and having the average lifetime of 1.25 ns and 1.41 ns, respectively. Whereas, in presence of the quencher i.e. Cu(II), a significant decrease of average lifetime was observed with a value of 0.66 ns. This data clearly signifies that it was a case of collisional deactivation or a typical example of dynamic quenching rather than the complexation mediated static quenching where the decrease of average lifetime may not be observed in presence of quencher [69].

In aqueous solution amino groups can efficiently bind with Cu(II) ion [70]. So, here we anticipated a non-radiative electron-transfer mechanism of Cu(II) ion mediated quenching of CDP3. The highest occupied molecular orbital (HOMO) and lowest unoccupied molecular (LUMO) energy levels of CDP3 can be estimated by the following equation [71,72]

$$\begin{aligned} E_{LUMO} &= -e(E_{Red} + 4.4) \\ E_{HOMO} &= -e(E_{Ox} + 4.4) \\ E_{HOMO} &= E_{LUMO} - E_g \end{aligned}$$

where, E_{Red} and E_{Ox} are the onset of reduction and oxidation potential, respectively for CD and CDP3. From Fig. 10b, E_{Red} is found to be -0.41 eV and -0.71 eV for CD and CDP3, respectively and the corresponding LUMO are found to be -3.99 eV and -3.67 eV. As the nature of oxidation is irreversible, the HOMO energy could not be established. Thus, HOMO energy level was determined by calculating the energy band gap (E_g), which is corresponding to the optical energy band gap and is found to be 5.85 for CDP3 (Table 3). The crystal field

stabilization energy (CFSE) of Cu(II) complex is obtained from Bossu et al. [73] and the calculated CFSE is 1.98 eV. In presence of Cu(II) ion, complexation between Cu(II) and amine groups of CDP3 led to split the d orbital of Cu(II) and results the electrons transfer from the excited state of CDP3 to the d orbital of Cu(II) as shown schematically in Fig. 10c. As transition of electron in the form of fluorescence emission was ceased which in turn leads to the quenching of fluorescence as in previous cases [53,74]. So, the predictable quenching mechanism of fluorescence of CDP3 was by the process of electron transfer.

4. Conclusion

In the present work, we have successfully synthesized CD from renewable source and conjugated it with PAMAM dendrimers with different generations. Among the CDP conjugates, CDP3 showed superior gene complexation capability and also gene protection capability against the enzymatic digestion. The low toxicity even up to 500 $\mu\text{g}/\text{ml}$ concentration, blood compatibility and improved gene transfection efficiency show promising gene delivery system for TNBC gene therapy. In addition to this, CDP3 showed highly selective detection of Cu(II) ion with a 93% fluorescence quenching efficiency and a detection copper ion concentration of 2 mM which could be useful to identify the metastases phase of triple negative breast cancer which exhibits higher level of Cu(II) ion. Therefore, CDP3 may be promising theranostic tool for TNBC in future.

Acknowledgement

This work is financially supported by DST-SERB funding agency through two sanctioned projects EEQ/2016/000712 and ECR/2016/002018. K.S. also acknowledge UGC for UGC-BSR Research Start-Up Grant (F.30-363/2017(BSR), Dt- 08/08/2017) and CU for UPE-II Nanofabrication project fund (UGC/166/UPE-II, Dt- 03/04/2017) for financial support. K.G also thanks to Pritiranjan Mondal for his help to prepare the manuscript.

Conflicts of interest

The authors declare no conflict of interest.

Appendix A. Supplementary data

Supplementary data to this article can be found online at <https://doi.org/10.1016/j.cej.2019.05.023>.

References

- [1] C. Statistics, Canadian cancer society's advisory committee on cancer statistics. in, Canadian Cancer Society, Canadian Cancer Society, 2015.
- [2] G. Mustacchi, M. De Laurentis, The role of taxanes in triple-negative breast cancer: literature review, *Drug Des. Dev. Therapy* 9 (2015) 4303.
- [3] S.I. Berndt, N.J. Camp, C.F. Skibola, J. Vijai, Z. Wang, J. Gu, A. Nieters, R.S. Kelly, K.E. Smedby, A. Monnereau, W. Cozen, A. Cox, S.S. Wang, Q. Lan, L.R. Teras, M. Machado, M. Yeager, A.R. Brooks-Wilson, P. Hartge, M.P. Purdue, B.M. Birmann, C.M. Vajdic, P. Cocco, Y. Zhang, G.G. Giles, A. Zeleniuch-Jacquotte, C. Lawrence, R. Montalvan, L. Burdett, A. Hutchinson, Y. Ye, T.G. Call, T.D. Shanafelt, A.J. Novak, N.E. Kay, M. Liebow, J.M. Cunningham, C. Allmer, H. Hjalgrim, H.-O. Adami, M. Melbye, B. Glimelius, E.T. Chang, M. Glenn, K. Curtin, L.A. Cannon-Albright, W.R. Diver, B.K. Link, G.J. Weiner, L. Conde, P.M. Bracci, J. Riby, D.K. Arnett, D. Zhi, J.M. Leach, E.A. Holly, R.D. Jackson, L.F. Tinker, Y. Benavente, N. Sala, D. Casabonne, N. Becker, P. Boffetta, P. Brennan, L. Foretova, M. Maynadie, J. McKay, A. Staines, K.G. Chaffee, S.J. Achenbach, C.M. Vachon, L.R. Goldin, S.S. Strom, J.F. Leis, J.B. Weinberg, N.E. Caporaso, A.D. Norman, A.J. De Roos, L.M. Morton, R.K. Severson, E. Riboli, P. Vineis, R. Kaaks, G. Masala, E. Weiderpass, M.-D. Chirlaque, R.C.H. Vermeulen, R.C. Travis, M.C. Southey, R.L. Milne, D. Albanes, J. Virtamo, S. Weinstein, J. Clavel, T. Zheng, T.R. Holford, D.J. Villano, A. Maria, J.J. Spinelli, R.D. Gascoyne, J.M. Connors, K.A. Bertrand, E. Giovannucci, P. Kraft, A. Krickler, J. Turner, M.G. Ennas, G.M. Ferri, L. Miligi, L. Liang, B. Ma, J. Huang, S. Crouch, J.-H. Park, N. Chatterjee, K.E. North, J.A. Snowden, J. Wright, J.F. Fraumeni, K. Offit, X. Wu, S. de Sanjose, J.R. Cerhan, S.J. Chanock, N. Rothman, S.L. Slager, Meta-analysis of genome-wide association studies

- discovers multiple loci for chronic lymphocytic leukemia, *Nat. Commun.* 7 (2016) 10933.
- [4] Y. Wang, T. Zhang, N. Kwiatkowski, B.J. Abraham, T.I. Lee, S. Xie, H. Yuzugullu, T. Von, H. Li, Z. Lin, CDK7-dependent transcriptional addiction in triple-negative breast cancer, *Cell* 163 (2015) 174–186.
- [5] G. MacDonald, I. Nalvarte, T. Smirnova, M. Vecchi, N. Aceto, A. Doelemeyer, A. Frei, S. Lienhard, J. Wyckoff, D. Hess, Memo, is a copper-dependent redox protein with an essential role in migration and metastasis, *Sci. Signal.* 7 (2014) ra56-ra56.
- [6] M. Yang, C.-Z. Huang, Mitogen-activated protein kinase signaling pathway and invasion and metastasis of gastric cancer, *World J. Gastroenterol.* 21 (2015) 11673.
- [7] J.T. Erler, K.L. Bennewith, T.R. Cox, G. Lang, D. Bird, A. Koong, Q.-T. Le, A.J. Giaccia, Hypoxia-induced lysyl oxidase is a critical mediator of bone marrow cell recruitment to form the premetastatic niche, *Cancer Cell* 15 (2009) 35–44.
- [8] M.A. Morrissey, R. Jayadev, G.R. Miley, C.A. Blebea, Q. Chi, S. Ihara, D.R. Sherwood, SPARC promotes cell invasion in vivo by decreasing type IV collagen levels in the basement membrane, *PLoS Genet.* 12 (2016) e1005905.
- [9] L. Finney, S. Mandava, L. Ursos, W. Zhang, D. Rodi, S. Vogt, D. Legnini, J. Maser, F. Ipkatt, O.I. Olopade, X-ray fluorescence microscopy reveals large-scale re-localization and extracellular translocation of cellular copper during angiogenesis, *Proc. Natl. Acad. Sci.* 104 (2007) 2247–2252.
- [10] V. Pavithra, T. Sathisha, K. Kasturi, D.S. Mallika, S.J. Amos, S. Ragunatha, Serum levels of metal ions in female patients with breast cancer, *J. Clin. Diagn. Res.: JC DR* 9 (2015) BC25.
- [11] K. Yang, L. Feng, X. Shi, Z. Liu, Nano-graphene in biomedicine: theranostic applications, *Chem. Soc. Rev.* 42 (2013) 530–547.
- [12] Z. Liu, X.-J. Liang, Nano-carbons as theranostics, *Theranostics* 2 (2012) 235.
- [13] S. Warner, *Diagnostics + Therapy = Theranostics, 2004.*
- [14] M.O. Ansari, M.F. Ahmad, G.G.H.A. Shadab, H.R. Siddique, Superparamagnetic iron oxide nanoparticles based cancer theranostics: a double edge sword to fight against cancer, *J. Drug Delivery Sci. Technol.* 45 (2018) 177–183.
- [15] S. Salman, H. Ashraf, S. Satya Ranjan, Iron oxide nanoparticles for breast cancer theranostics, *Curr. Drug Metab.* 20 (2019) 1–11.
- [16] A. Mashal, B. Sitharaman, X. Li, P.K. Avti, A.V. Sahakian, J.H. Booske, S.C. Hagness, Toward carbon-nanotube-based theranostic agents for microwave detection and treatment of breast cancer: enhanced dielectric and heating response of tissue-mimicking materials, *IEEE Trans. Biomed. Eng.* 57 (2010) 1831–1834.
- [17] S.P. Singh, Multifunctional magnetic quantum dots for cancer theranostics, *J. Biomed. Nanotechnol.* 7 (2011) 95–97.
- [18] A. Gharatape, R. Salehi, Recent progress in theranostic applications of hybrid gold nanoparticles, *Eur. J. Med. Chem.* 138 (2017) 221–233.
- [19] M. Singh, D.C.C. Harris-Birtill, S.R. Markar, G.B. Hanna, D.S. Elson, Application of gold nanoparticles for gastrointestinal cancer theranostics: a systematic review, *Nanomed.: Nanotechnol. Biol. Med.* 11 (2015) 2083–2098.
- [20] K. Ghosal, K. Sarkar, Biomedical applications of graphene nanomaterials and beyond, *ACS Biomater. Sci. Eng.* 4 (2018) 2653–2703.
- [21] M.W. Ambrogio, C.R. Thomas, Y.-L. Zhao, J.I. Zink, J.F. Stoddart, Mechanized silica nanoparticles: a new frontier in theranostic nanomedicine, *Acc. Chem. Res.* 44 (2011) 903–913.
- [22] S.-H. Cheng, C.-H. Lee, M.-C. Chen, J.S. Souris, F.-G. Tseng, C.-S. Yang, C.-Y. Mou, C.-T. Chen, L.-W. Lo, Tri-functionalization of mesoporous silica nanoparticles for comprehensive cancer theranostics—the trio of imaging, targeting and therapy, *J. Mater. Chem.* 20 (2010) 6149–6157.
- [23] I. Khan, K. Saeed, I. Khan, Nanoparticles: properties, applications and toxicities, *Arabian J. Chem.* (2017).
- [24] L. Yildirim, N.T.K. Thanh, M. Loizidou, A.M. Seifalian, Toxicology and clinical potential of nanoparticles, *Nano Today* 6 (2011) 585–607.
- [25] A. Prasannan, T. Imae, One-pot synthesis of fluorescent carbon dots from orange waste peels, *Ind. Eng. Chem. Res.* 52 (2013) 15673–15678.
- [26] K. Sarkar, P.P. Kundu, Preparation of low molecular weight N-maleated chitosan-graft-PAMAM copolymer for enhanced DNA complexation, *Int. J. Biol. Macromol.* 51 (2012) 859–867.
- [27] K. Sarkar, S.L. Banerjee, P.P. Kundu, G. Madras, K. Chatterjee, Biofunctionalized surface-modified silver nanoparticles for gene delivery, *J. Mater. Chem. B* 3 (2015) 5266–5276.
- [28] K. Sarkar, G. Madras, K. Chatterjee, Dendron conjugation to graphene oxide using click chemistry for efficient gene delivery, *RSC Adv.* 5 (2015) 50196–50211.
- [29] K. Sarkar, S.R.K. Meka, G. Madras, K. Chatterjee, A self-assembling polycationic nanocarrier that exhibits exceptional gene transfection efficiency, *RSC Adv.* 5 (2015) 91619–91632.
- [30] S. Kumar, S. Raj, K. Sarkar, K. Chatterjee, Engineering a multi-biofunctional composite using poly (ethyleneimine) decorated graphene oxide for bone tissue regeneration, *Nanoscale* 8 (2016) 6820–6836.
- [31] A.B. Bourlinos, A. Stassinopoulos, D. Anglos, R. Zboril, V. Georgakilas, E.P. Giannelis, Photoluminescent carbonogenic dots, *Chem. Mater.* 20 (2008) 4539–4541.
- [32] J. Zhang, W. Shen, D. Pan, Z. Zhang, Y. Fang, M. Wu, Controlled synthesis of green and blue luminescent carbon nanoparticles with high yields by the carbonization of sucrose, *New J. Chem.* 34 (2010) 591–593.
- [33] C.-W. Lai, Y.-H. Hsiao, Y.-K. Peng, P.-T. Chou, Facile synthesis of highly emissive carbon dots from pyrolysis of glycerol; gram scale production of carbon dots/mSiO₂ for cell imaging and drug release, *J. Mater. Chem.* 22 (2012) 14403–14409.
- [34] A. Emam, S.A. Loutfy, A.A. Mostafa, H. Awad, M.B. Mohamed, Cyto-toxicity, biocompatibility and cellular response of carbon dots—plasmonic based nano-hybrids for bioimaging, *RSC Adv.* 7 (2017) 23502–23514.
- [35] S. Qu, X. Wang, Q. Lu, X. Liu, L. Wang, A biocompatible fluorescent ink based on water-soluble luminescent carbon nanodots, *Angew. Chem. Int. Ed.* 51 (2012) 12215–12218.
- [36] D. Gu, P. Zhang, L. Zhang, H. Liu, Z. Pu, S. Shang, Nitrogen and phosphorus co-doped carbon dots derived from lily bulbs for copper ion sensing and cell imaging, *Opt. Mater.* 83 (2018) 272–278.
- [37] Y. Liu, Y. Zhao, Y. Zhang, One-step green synthesized fluorescent carbon nanodots from bamboo leaves for copper(II) ion detection, *Sens. Actuators, B* 196 (2014) 647–652.
- [38] P. Mondal, K. Ghosal, S.K. Bhattacharyya, M. Das, A. Bera, D. Ganguly, P. Kumar, J. Dwivedi, R. Gupta, A.A. Martí, Formation of a gold-carbon dot nanocomposite with superior catalytic ability for the reduction of aromatic nitro groups in water, *RSC Adv.* 4 (2014) 25863–25866.
- [39] P. Jana, K. Sarkar, T. Mitra, A. Chatterjee, A. Gnanamani, G. Chakraborti, P. Kundu, Synthesis of a carboxymethylated guar gum grafted polyethyleneimine copolymer as an efficient gene delivery vehicle, *RSC Adv.* 6 (2016) 13730–13741.
- [40] C.Y.M. Hsu, H. Uludağ, Effects of size and topology of DNA molecules on intracellular delivery with non-viral gene carriers, *BMC Biotech.* 8 (2008) 23–24.
- [41] C. Kneuer, C. Ehrhardt, H. Bakowsky, M. Ravi Kumar, V. Oberle, C.M. Lehr, D. Hoekstra, U. Bakowsky, The influence of physicochemical parameters on the efficacy of non-viral DNA transfection complexes: a comparative study, *J. Nanosci. Nanotechnol.* 6 (2006) 2776–2782.
- [42] P.-C. Hsu, P.-C. Chen, C.-M. Ou, H.-Y. Chang, H.-T. Chang, Extremely high inhibition activity of photoluminescent carbon nanodots toward cancer cells, *J. Mater. Chem. B* 1 (2013) 1774–1781.
- [43] E. Fröhlich, The role of surface charge in cellular uptake and cytotoxicity of medical nanoparticles, *Int. J. Nanomed.* 7 (2012) 5577.
- [44] S. Pöyry, I. Vattulainen, Role of charged lipids in membrane structures — insight given by simulations, *Biochimica et Biophysica Acta (BBA) – Biomembranes* 1858 (2016) 2322–2333.
- [45] U. Lungwitz, M. Breunig, T. Blunk, A. Göpferich, Polyethyleneimine-based non-viral gene delivery systems, *Eur. J. Pharm. Biopharm.* 60 (2005) 247–266.
- [46] Naked DNA Gene Transfer, *Molecular Therapy* 1 (2000) S221–S232.
- [47] M.S. Al-Dosari, X. Gao, Nonviral gene delivery: principle, limitations, and recent progress, *AAPS J.* 11 (2009) 671–681.
- [48] K. Sarkar, A. Chatterjee, G. Chakraborti, P.P. Kundu, Blood compatible N-maleyl chitosan-graft-PAMAM copolymer for enhanced gene transfection, *Carbohydr. Polym.* 98 (2013) 596–606.
- [49] L. Jin, X. Zeng, M. Liu, Y. Deng, N. He, Current progress in gene delivery technology based on chemical methods and nano-carriers, *Theranostics* 4 (2014) 240–255.
- [50] P.P. Karmali, A. Chaudhuri, Cationic liposomes as non-viral carriers of gene medicines: resolved issues, open questions, and future promises, *Med. Res. Rev.* 27 (2007) 696–722.
- [51] P.-H. Wu, Y. Onodera, Y. Ichikawa, E.B. Rankin, A.J. Giaccia, Y. Watanabe, W. Qian, T. Hashimoto, H. Shirato, J.-M. Nam, Targeting integrins with RGD-conjugated gold nanoparticles in radiotherapy decreases the invasive activity of breast cancer cells, *Int. J. Nanomed.* 12 (2017) 5069–5085.
- [52] Y. Dong, R. Wang, G. Li, C. Chen, Y. Chi, G. Chen, Polyamine-functionalized carbon quantum dots as fluorescent probes for selective and sensitive detection of copper ions, *Anal. Chem.* 84 (2012) 6220–6224.
- [53] J. Wang, R.S. Li, H.Z. Zhang, N. Wang, Z. Zhang, C.Z. Huang, Highly fluorescent carbon dots as selective and visual probes for sensing copper ions in living cells via an electron transfer process, *Biosens. Bioelectron.* 97 (2017) 157–163.
- [54] V. Singh, V. Kumar, U. Yadav, R.K. Srivastava, V.N. Singh, A. Banerjee, S. Chakraborty, A.K. Shukla, D.K. Misra, R. Ahuja, A. Srivastava, P.S. Saxena, Sensitive and selective detection of copper ions using low cost nitrogen doped carbon quantum dots as a fluorescent sensing platform, *ISSS Journal of Micro and Smart Systems* 6 (2017) 109–117.
- [55] Q. Liu, N. Zhang, H. Shi, W. Ji, X. Guo, W. Yuan, Q. Hu, One-step microwave synthesis of carbon dots for highly sensitive and selective detection of copper ions in aqueous solution, *New Journal of Chemistry* 42 (2018) 3097–3101.
- [56] J. Chen, Y. Li, K. Lv, W. Zhong, H. Wang, Z. Wu, P. Yi, J. Jiang, Cyclam-functionalized carbon dots sensor for sensitive and selective detection of copper(II) ion and sulfide anion in aqueous media and its imaging in live cells, *Sensors and Actuators B: Chemical* 224 (2016) 298–306.
- [57] P. Das, S. Ganguly, M. Bose, S. Mondal, A.K. Das, S. Banerjee, N.C. Das, A simplistic approach to green future with eco-friendly luminescent carbon dots and their application to fluorescent nano-sensor β -turn-off β ™ probe for selective sensing of copper ions, *Materials Science and Engineering: C* 75 (2017) 1456–1464.
- [58] M. Ganiga, J. Cyriac, Understanding the Photoluminescence Mechanism of Nitrogen-Doped Carbon Dots by Selective Interaction with Copper Ions, *ChemPhysChem* 17 (2016) 2315–2321.
- [59] F. Wang, Z. Gu, W. Lei, W. Wang, X. Xia, Q. Hao, Graphene quantum dots as a fluorescent sensing platform for highly efficient detection of copper(II) ions, *Sensors and Actuators B: Chemical* 190 (2014) 516–522.
- [60] L. Finney, S. Vogt, T. Fukai, D. Glesne, Copper and angiogenesis: unravelling a relationship key to cancer progression, *Clin. Exp. Pharmacol. Physiol.* 36 (2009) 88–94.
- [61] D.C. Brady, M.S. Crowe, M.L. Turski, G.A. Hobbs, X. Yao, A. Chaikuad, S. Knapp, K. Xiao, S.L. Campbell, D.J. Thiele, C.M. Counter, Copper is required for oncogenic BRAF signaling and tumorigenesis, *Nature* 509 (2014) 492.
- [62] S.S. Brem, D. Zagzag, A. Tsanaclis, S. Gately, M. Elkouby, S. Brien, Inhibition of angiogenesis and tumor growth in the brain. Suppression of endothelial cell turnover by penicillamine and the depletion of copper, an angiogenic cofactor, *Am. J. Pathol.* 137 (1990) 1121.
- [63] S. Ishida, P. Andreux, C. Poitry-Yamate, J. Auwerx, D. Hanahan, Bioavailable copper modulates oxidative phosphorylation and growth of tumors, *Proc. Natl.*

- Acad. Sci. 110 (2013) 19507–19512.
- [64] L.Q. Chen, M.D. Pagel, Evaluating pH in the extracellular tumor microenvironment using CEST MRI and other imaging methods, *Adv. Radiol.* 2015 (2015) 206405.
- [65] Y. Kato, S. Ozawa, C. Miyamoto, Y. Maehata, A. Suzuki, T. Maeda, Y. Baba, Acidic extracellular microenvironment and cancer, *Cancer Cell Int.* 13 (2013) 89–90.
- [66] Y. Chen, Z. Rosenzweig, Luminescent CdS quantum dots as selective ion probes, *Anal. Chem.* 74 (2002) 5132–5138.
- [67] X. Wu, S. Sun, Y. Wang, J. Zhu, K. Jiang, Y. Leng, Q. Shu, H. Lin, A fluorescent carbon-dots-based mitochondria-targetable nanoprobe for peroxynitrite sensing in living cells, *Biosens. Bioelectron.* 90 (2017) 501–507.
- [68] H.X. Zhao, L.Q. Liu, Z.D. Liu, Y. Wang, X.J. Zhao, C.Z. Huang, Highly selective detection of phosphate in very complicated matrixes with an off-on fluorescent probe of europium-adjusted carbon dots, *Chem. Commun.* 47 (2011) 2604–2606.
- [69] F. Wang, Z. Gu, W. Lei, W. Wang, X. Xia, Q. Hao, Graphene quantum dots as a fluorescent sensing platform for highly efficient detection of copper (II) ions, *Sens. Actuators, B* 190 (2014) 516–522.
- [70] Y. Lin, H. Chen, K. Lin, B. Chen, C. Chiou, Application of magnetic particles modified with amino groups to adsorb copper ions in aqueous solution, *J. Environ. Sci.* 23 (2011) 44–50.
- [71] B. Liang, C. Jiang, Z. Chen, X. Zhang, H. Shi, Y. Cao, New iridium complex as high-efficiency red phosphorescent emitter in polymer light-emitting devices, *J. Mater. Chem.* 16 (2006) 1281–1286.
- [72] M.J. Cho, J.-I. Jin, D.H. Choi, J.H. Yoon, C.S. Hong, Y.M. Kim, Y.W. Park, B.-K. Ju, Tunable emission of polymer light emitting diodes bearing green-emitting Ir(III) complexes: the structural role of 9-((6-(4-fluorophenyl)pyridin-3-yl)methyl)-9H-carbazole ligands, *Dyes Pigm.* 85 (2010) 143–151.
- [73] F.P. Bossu, K.L. Chellappa, D.W. Margerum, Ligand effects on the thermodynamic stabilization of copper(III)-peptide complexes, *J. Am. Chem. Soc.* 99 (1977) 2195–2203.
- [74] H. Zhang, Y. Chen, M. Liang, L. Xu, S. Qi, H. Chen, X. Chen, Solid-phase synthesis of highly fluorescent nitrogen-doped carbon dots for sensitive and selective probing ferric ions in living cells, *Anal. Chem.* 86 (2014) 9846–9852.